



VYSOKÉ UČENÍ TECHNICKÉ V BRNĚ
BRNO UNIVERSITY OF TECHNOLOGY



FAKULTA STROJNÍHO INŽENÝRSTVÍ
ÚSTAV FYZIKÁLNÍHO INŽENÝRSTVÍ
FACULTY OF MECHANICAL ENGINEERING
INSTITUTE OF PHYSICAL ENGINEERING

MAGNETIC TRANSFORMATION OF METASTABLE FCC FE/CU(100) FILMS BY FOCUSED ION BEAM

MAGNETICKÁ TRANSFORMACE METASTABILNÍCH VRSTEV FCC FE/CU(100) POMOCÍ
FOKUSOVANÉHO IONTOVÉHO SVAZKU

DIPLOMOVÁ PRÁCE
MASTER'S THESIS

AUTOR PRÁCE
AUTHOR

Bc. JONÁŠ GLOSS

VEDOUCÍ PRÁCE
SUPERVISOR

Ing. MICHAL URBÁNEK, Ph.D.

Vysoké učení technické v Brně, Fakulta strojního inženýrství

Ústav fyzikálního inženýrství

Akademický rok: 2013/2014

ZADÁNÍ DIPLOMOVÉ PRÁCE

student(ka): Bc. Jonáš Gloss

který/která studuje v **magisterském navazujícím studijním programu**

obor: **Fyzikální inženýrství a nanotechnologie (3901T043)**

Ředitel ústavu Vám v souladu se zákonem č.111/1998 o vysokých školách a se Studijním a zkušebním řádem VUT v Brně určuje následující téma diplomové práce:

Magnetická transformace metastabilních vrstev fcc Fe/Cu(100) pomocí fokusovaného iontového svazku

v anglickém jazyce:

Magnetic transformation of metastable fcc Fe/Cu(100) films by focused ion beam

Stručná charakteristika problematiky úkolu:

Magnetické nanostruktury mají obrovský potenciál v oblasti záznamu dat a ve vývoji nových nanomagnetických zařízení. Přímá tvorba magnetických nanostruktur pomocí iontového nebo elektronového ozařování je jednokrokový proces, což představuje výhodu oproti běžným litografickým technikám. Cílem diplomové práce je připravit vrstvy vhodné pro magnetickou transformaci fokusovaným iontovým svazkem a demonstrovat na nich možnost tvorby magnetických nanostruktur.

Cíle diplomové práce:

Proveďte rešeršní studii týkající se tvorby magnetických nanostruktur iontovým ozařováním.

Připravte vrstvy metastabilního fcc Fe/Cu(100) vhodné pro iontovou transformaci a charakterizujte jejich strukturní a magnetické vlastnosti.

Pomocí fokusovaného iontového svazku připravte nanostruktury v metastabilních vrstvách a charakterizujte jejich vlastnosti.

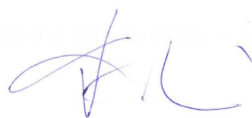
Seznam odborné literatury:

J. FASSBENDER, J. McCORD, Magnetic patterning by ion beam irradiation“ J. Magn. Magn. Mater. 320 (2008) 579-596.

Vedoucí diplomové práce: Ing. Michal Urbánek, Ph.D.

Termín odevzdání diplomové práce je stanoven časovým plánem akademického roku 2013/2014.

V Brně, dne 22.11.2013



prof. RNDr. Tomáš Šikola, CSc.
Ředitel ústavu



prof. RNDr. Miroslav Doupovec, CSc., dr. h. c.
Děkan fakulty

Abstrakt

Metastabilní tenké vrstvy paramagnetického, plošně centrovaného kubického (fcc) Fe připravené na monokrystalu Cu(100) jsou dobrými kandidáty pro tvorbu magnetických struktur pomocí fokusovaného iontového svazku díky jejich magnetické a strukturní fázové transformaci na feromagnetické, prostorově centrované (bcc) Fe po ozáření ionty. Problémem bylo, že tenké vrstvy čistého fcc Fe se spontánně transformují, když jejich tloušťka přesáhne 10 monovrstev. Tato hranice může být posunuta na 22 monovrstev, když se depozice Fe provede v atmosféře CO. Ukázali jsme, že je možné růst mnohem tlustší vrstvy pomocí legování s Ni, který stabilizuje fcc fázi. Zjistili jsme množství Ni, které je potřebné k stabilizaci nemagnetického, metastabilního fcc Fe a popsali jsme jeho závislost na tlaku v komoře během depozice ve fázovém diagramu, který ukazuje metastabilní region. Rovněž jsme ukázali, že stabilizující efekt zvýšeného tlaku v komoře se může odstranit pomocí saturace povrchu O a proto mohou být metastabilní vrstvy připraveny také v depozičních systémech s vyšším základním tlakem. Nakonec jsme ukázali tvorbu mikro- a nanostruktur ve 44 ML hrubých vrstvách Fe legovaného s Ni na Cu(100) pomocí fokusovaného iontového svazku.

Abstract

Metastable paramagnetic face-centered cubic (fcc) Fe thin films deposited on a Cu(100) single-crystal are good candidates for focused ion-beam magnetic patterning, due to their structural and magnetic phase transformation to ferromagnetic body-centered cubic (bcc) Fe upon ion-beam irradiation. However, pure fcc Fe films undergo spontaneous transformation when their thickness exceeds 10 ML. This limit can be extended to approximately 22 ML by deposition of Fe at increased CO background pressures. We show that much thicker films can be grown by alloying with Ni, that stabilizes the fcc phase. The amount of Ni necessary to stabilize non-magnetic, metastable fcc Fe films in dependence on the residual background pressure during the deposition is determined and a phase diagram revealing the metastable region is presented. It is also shown that the stabilizing effect of CO can be removed by artificial O saturation of the surface and thus the Ni-stabilized films can be grown also in systems with lower vacuum. Finally, we present fabrication of micro- and nanostructures in 44 ML thick films of Fe alloyed with Ni on Cu(100) by focused ion beam.

Klíčová slova

metastabilní vrstvy, magnetické struktury, magnetická transformace, stabilizující efekt, legování, fokusovaný iontový svazek

Keywords

metastable films, magnetic structures, magnetic transformation, stabilizing effect, alloying, focused ion beam

GLOSS, J. *Magnetic transformation of metastable fcc Fe/Cu(100) films by focused ion beam*. Brno: Vysoké učení technické v Brně, Fakulta strojního inženýrství, 2014. 54 s. Vedoucí Ing. Michal Urbánek, Ph.D.

Prohlášení

Prohlašuji, že svou diplomovou práci na téma "Magnetická transformace metastabilních vrstev fcc Fe/Cu(100) pomocí fokusovaného iontového svazku" jsem vypracoval samostatně pod vedením vedoucího diplomové práce a s použitím odborné literatury a dalších informačních zdrojů, které jsou všechny citovány v práci a uvedeny v seznamu literatury na konci práce.

Jako autor uvedené diplomové práce dále prohlašuji, že v souvislosti s vytvořením této diplomové práce jsem neporušil autorská práva třetích osob, zejména jsem nezasáhl nedovoleným způsobem do cizích autorských práv osobnostních a jsem si plně vědom následků porušení ustanovení § 11 a následujících autorského zákona č. 121/2000 Sb., včetně možných trestněprávních důsledků vyplývajících z ustanovení § 152 trestního zákona č. 140/1961 Sb.

Bc. Jonáš Gloss

Acknowledgements

My foremost gratitude belongs to my supervisor Dr. Michal Urbánek, whose approach to this project inspired me a great deal. Working with him was always both enriching and exciting. The work presented in this thesis is a result of a wonderful collaboration of the Brno University of Technology and the TU Wien. I would like to thank prof. Šíkola, prof. Diebold and prof. Varga for their support for both me and this joint project. I would also like to convey my gratefulness to prof. Varga and prof. Schmid for sharing their supreme experimental and theoretical overview of the system Fe/Cu(100). I furthermore want to express my appreciation to Dr. Z, who showed me how to SMOKE and gave me a great deal of valuable advice that numerous times saved the UHV in the PINUP. Moreover, I enjoyed working alongside Ing. Pavelec, with whom I was able to share my latest results in the latest hours. Finally, I must note that most of the MFM measurements in this thesis could not have been performed without the assistance of my colleague, Ing. Staňo.

Ďakujem tiež svojim kolegom, zvlášť Ing. Hulvovi, Ing. Marešovi a Ing. Měchovi, za spoločné štúdium a neoceniteľné rady do života. Nakoniec ďakujem saleziánom v Brne-Žabovřeskách a vo Viedni a svojej rodine za poskytnutie skvelého zázemia, ktoré vyvažovalo dlhé hodiny strávené v laboratóriu a dovolilo mi venovať sa skúmaniu (Ž 8).

Bc. Jonáš Gloss

Contents

1	Introduction	3
2	Thin film deposition and characterization	4
2.1	Molecular Beam Epitaxy	4
2.2	Auger Electron Spectroscopy	6
2.3	Low Energy Electron Diffraction	8
2.4	Magnetism	9
2.4.1	Categories of magnetic materials	9
2.4.2	Magnetic anisotropy	10
2.4.3	Multi-layer systems	10
2.5	Magneto-Optical Kerr Effect	11
2.6	Deposition of thin iron films	12
2.6.1	Pure iron films	12
2.6.2	Ion beam irradiation of pure iron films	14
2.6.3	Growth of iron films in carbon monoxide	15
2.6.4	Growth of alloys of iron with nickel	16
3	Patterning and characterization of magnetic nanostructures	20
3.1	Theoretical background and techniques	20
3.1.1	Atomic and Magnetic Force Microscopies	20
3.1.2	Focused Ion Beam and Scanning Electron Microscopy	22
3.2	Magnetic nanostructures in magnetic films	22
3.3	Magnetic nanostructures in non-magnetic films	25
4	Deposition of thin $\text{Fe}_x\text{Ni}_{1-x}/\text{Cu}$ films	27
4.1	Sample Preparation	27
4.2	Deposition	27
4.3	Growth of metastable $\text{Fe}_{85}\text{Ni}_{15}/\text{Cu}(100)$	29
4.4	Growth of metastable $\text{Fe}_x\text{Ni}_{1-x}/\text{Cu}(100)$	32
4.5	Phase diagram of Fe and Ni	33
5	The effect of CO and O₂ on growth of 44 ML $\text{Fe}_{78}\text{Ni}_{22}$ films	35
5.1	Saturation of O in order to prevent the stabilizing CO effect	35
5.1.1	The film grown in 1×10^{-9} millibar CO	35
5.1.2	The film grown in 1×10^{-9} millibar CO, artificial O saturation after 11 ML	36
5.1.3	The film grown in 1×10^{-9} millibar CO, artificial oxygen saturation after 22 ML	39
5.1.4	The film grown in 3×10^{-9} millibar CO	40
5.2	Summary of the effect of CO and O on the $\text{Fe}_{78}\text{Ni}_{22}$	40
6	Magnetic Nanostructures in 44 ML $\text{Fe}_{78}\text{Ni}_{22}$ films	43
6.1	Magnetic nanostructures created by 30 keV Gallium ions	44
6.1.1	Different size of patterns with different dose	44
6.1.2	Different ion dose and irradiation parameters	47

CONTENTS

6.2	Magnetic nanostructures created by 10 keV Gallium ions	48
7	Conclusion	51

1. Introduction

Nanoscale magnetic patterning has a great potential for ultrahigh-density magnetic recording and in the development of novel nano-magnetic devices and systems. Direct writing of magnetic patterns by focused ion- or electron-beam irradiation is a single-step process, which is an advantage over traditional multi-step lithography techniques.

In previous works on ion-induced magnetic patterning on the system we will investigate in this thesis, the crystallographic structure was modified by ion bombardment (fcc to bcc), changing the magnetization (non-magnetic to ferromagnetic) of the material [1, 2, 3, 4, 5]. Transformation from a non-magnetic to a ferromagnetic state is most desirable for applications, making it possible to write arbitrary magnetic patterns that are magnetically “isolated” by non-magnetic regions.

The objective of this work was to fabricate magnetic nanostructures in thin films of Fe alloyed with Ni on Cu(100). We make a clear distinction between fabrication and treatment of the thin films and the fabrication of magnetic nanostructures in these films. For this reason, the first two chapters are divided, because the first one deals with the thin film deposition and characterisation and the second one with the nano-patterning of the films.

To understand the topics covered in the thesis which will eventually lead to creation of magnetic nanostructures, we will begin with a theoretical section. This will include the description of thin film growth and some of the techniques commonly used for thin film characterization.

After this a review of the previous investigation of a system of Fe/Cu(100) will follow. The first chapter will then be concluded with the latest measurements on the Fe-Ni alloys. The second chapter is written as a review of different methods of nano-patterning and is concluded with an example of nano-patterning of the Fe/Cu(100) system.

After the introduction into experimental techniques and existing systems suitable for magnetic patterning by ion beam irradiation, an investigation of $\text{Fe}_x\text{Ni}_{1-x}$ alloys and the interplay with chamber pressure will follow in the third chapter. In conclusion to this chapter a phase diagram of dependence of film stability on Ni concentration and the chamber pressure will be presented. The results of this chapter have already been published in [6]. The fourth chapter will focus on application of this research to different vacuum systems, with a final aim of moving the growth from the TU Wien to the laboratories of the Institute of Physical Engineering at the Faculty of Mechanical Engineering of the Brno University of Technology.

The final chapter of this diploma thesis aims to give an account on the creation of nanostructures in the films which we have grown and some interesting phenomena we have observed will be discussed.

2. Thin film deposition and characterization

The purpose of this chapter is introduction to thin film deposition by evaporation, description of some of the techniques used for their characterization and finally to acquaint the reader with the main topic of this thesis: deposition of Fe alloyed with Ni on Cu(100).

The first mention of thin film deposition is by Michael Faraday [7]. In 1857, Faraday produced evaporated thin films when experimenting with exploding fuse-like metal wires in an inert atmosphere. The objective of a deposition is to controllably transfer atoms from a source to a substrate where film formation and growth proceed atomistically. In evaporation, atoms are removed from the source by thermal means. A typical evaporator used today is described in figure 2.1. Films prepared in this manner are therefore appropriate candidates for characterization via e.g. Auger Electron Spectroscopy, Low Energy Electron Diffraction and Magneto-Optical Kerr Effect, which will also be described in this chapter.

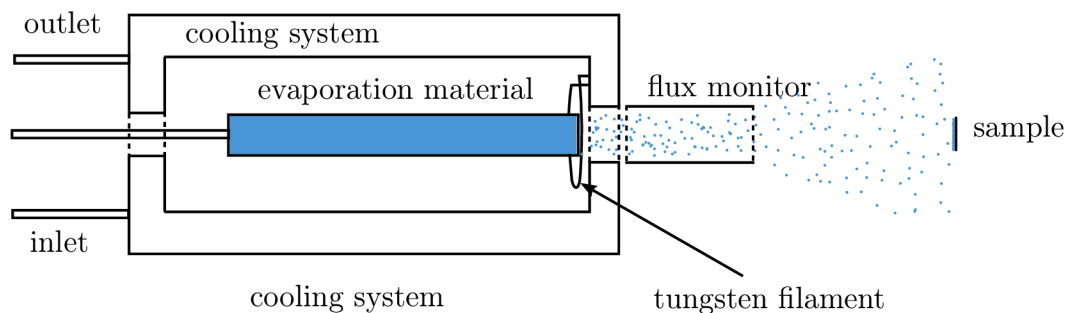


Figure 2.1: Scheme of an Omicron EFM3 evaporator. The evaporation material is heated by electrons emitted from tungsten filament and accelerated by potential difference. Atoms that leave the evaporation rod spread out and only a very small portion of them hits the sample. Some of the atoms of the evaporated material are ionized and these ions from are measured by flux monitor. The body of evaporator has to be cooled due to the high temperatures involved in the process.

2.1. Molecular Beam Epitaxy

Two ancient Greek words $\epsilon\phi\upsilon$ (epi - placed or resting upon) and $\tau\alpha\xi\iota\zeta$ (taxis - arrangement) are the root of the modern word *epitaxy*, which describes an extremely important phenomenon exhibited by thin films. Epitaxy refers to extended single-crystal film formation on top of a crystalline substrate. It was probably first observed to occur in alkali halide crystals over a century ago, but the actual word epitaxy was introduced to literature by a French mineralogist L. Royer in 1928 [8]. Two types of epitaxy can be distinguished and each has important scientific and technological implications. Homoepitaxy refers to growth of a film consisting of the same material as the substrate. Heteroepitaxy is the more common type and refers to the case where the film and substrate consist of different materials. For example, optoelectronic devices such as light-emitting diodes and lasers are

2. THIN FILM DEPOSITION AND CHARACTERIZATION

based on compound semiconductor heteroepitaxial film structures, and so is the system we investigated in this thesis.

There are various factors associated with the growth process of an evaporated material on a substrate. Three modes are distinguished when considering the growth of films thicker than one monolayer (ML).

First is the layer-by-layer growth, which is characterized by growth of consecutive full MLs. The reason for this is a stronger interaction between the substrate and the atoms of the layer in comparison to the interaction between the atoms in a layer. This growth is also known as the Frank-van der Merwe growth and is shown in figure 2.2(a). The system investigated in this thesis [$\text{Fe}_x\text{Ni}_{1-x}/\text{Cu}(100)$] is known to grow in this manner.

Secondly, it is the layer-and-island growth [see figure 2.2(b)] which is defined by growth of islands on full MLs. These islands usually connect as they grow and thus create other MLs. This mode is observed either when the lattice parameter of the film is different from that of the substrate, or when the symmetry (orientation) of the film is not energetically favorable with respect to the crystal lattice of the substrate. These factors result in a behavior such that after evaporation of several layers the strain in the bulk becomes too large. The layer-by-layer growth is then destroyed and small islands are formed. This mode is also called the Stransky-Krastanov mode. [9]

Finally, we recognize the island growth mode, in which the evaporated material grows in islands with no MLs formed, because the interaction between the atoms is stronger than between the atoms and the substrate. It is also known as the Volmer-Weber growth mode and is shown in figure 2.2(c).

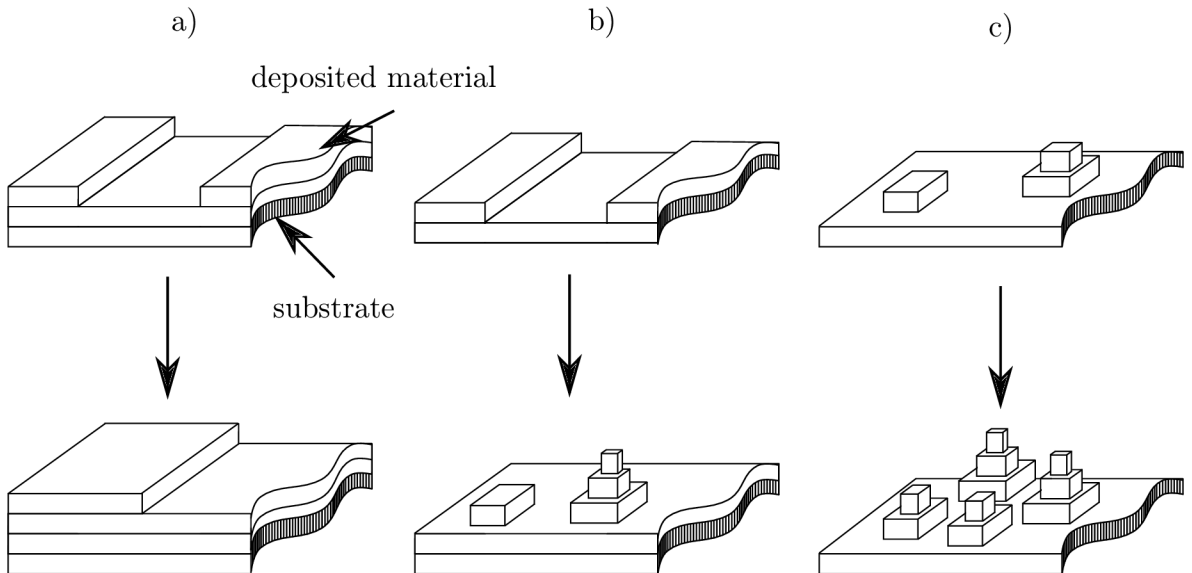


Figure 2.2: The main growth modes. (a) shows the layer-by-layer growth, (b) depicts the layer-and-island growth and (c) the island growth.

2.2. Auger Electron Spectroscopy

Auger Electron Spectroscopy (AES) is often used for chemical surface analysis of conducting samples in Ultra High Vacuum (UHV). The process consists of ionization of the studied surface and respective analysis of the emitted electrons. The ionization is done by electrons with an energy between 3 and 30 keV. Collision of the electrons with the surface results in their absorption or reflection (figure 2.3), which could consist of either elastic or inelastic collisions. The latter could then lead to emission of secondary electrons; part of this spectra are the Auger electrons. Because they have a characteristic energy, they allow us to identify the emitting elements.

Figure 2.3 shows the schematic view of how the Auger electrons are emitted. It can be seen that the energy of the Auger electrons is independent of the energy of the incident electrons and can be expressed:

$$E_{\text{Auger}} = E_1 - E_2 - E_3 \quad (2.1)$$

where

- E_{Auger} is the kinetic energy of an Auger electron,
- E_1 is the binding energy of an electron that is emitted from the core of the atom (K shell),
- E_2 is the binding energy of the filling electron, which substitutes the electron emitted from the core (KL transition),
- E_3 is the binding energy of the Auger electron.

In the figure it is shown that the process begins with the incident electron. The system absorbs a well-specified energy E_1 , which is then consumed by the consequent KL electron transition ($E_1 - E_2$) and Auger electron emission (E_{Auger}).

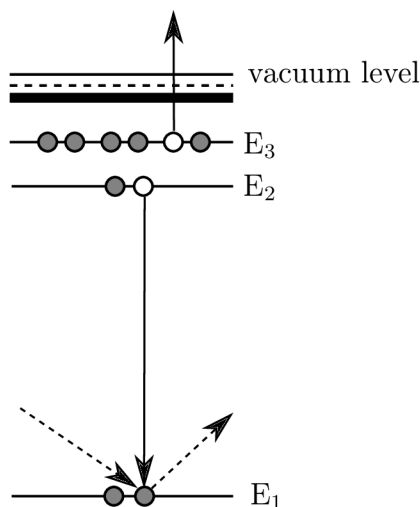


Figure 2.3: Schematic view of energy levels inside an atom (E_{1-3}) and of the Auger electrons' emission process.

2. THIN FILM DEPOSITION AND CHARACTERIZATION

AES analysis can to some extent be used for quantitative analysis of the elements present in the sample. Because Auger electrons are emitted essentially from the first 2-10 ML [10], AES is a surface sensitive method and can therefore be very well used for the purpose of quantifying the composition of the Fe_xNi_{1-x} thin films, which will be thoroughly investigated as a part of this thesis. AES can also be used after sample cleaning procedure to check the purity of the Cu(100) surface.

The probability of emission of the Auger electrons varies with elements. Figure 2.4 shows the respective sensitivity factors for different elements. The concentration is then estimated from equation 2.2. In this equation, x stands for an element which concentration we aim to calculate and i encompasses all of the elements that are in a measured Auger spectra. I is the measured APPH and S is the sensitivity factor of an element.

$$C_x = \frac{\frac{I_x}{S_x}}{\sum \frac{I_i}{S_i}} \quad (2.2)$$

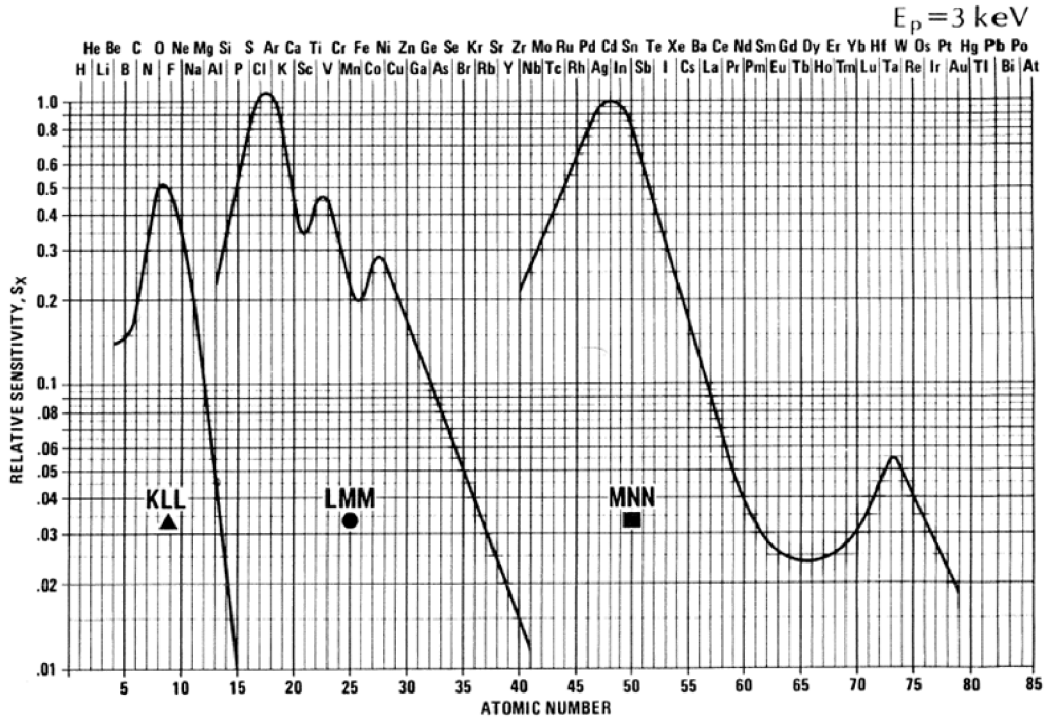


Figure 2.4: Auger Electron Spectroscopy relative sensitivities for electrons with energy 3 keV [11].

2.3. LOW ENERGY ELECTRON DIFFRACTION

2.3. Low Energy Electron Diffraction

In the 1920s, Davisson and Germer observed diffraction effects of electrons backscattered from a single crystal of Ni [12]. This method has later on been named as Low Energy Electron Diffraction (LEED) and is a frequently used technique in surface science. We will use the reciprocal space to describe the behaviour of diffracted electrons and the creation of a diffraction pattern.

Let us use a crystal lattice with atomic distances a and an incident electron with a wavelength λ . Further we shall assume that the reciprocal (atomic) distances $||\vec{k}_a|| = 2\pi/a$ are proportional to the wavenumber of an incident electron $||\vec{k}|| = 2\pi/\lambda$. The energy of the incident electron with momentum $p = \hbar/k_0$ is:

$$E = \frac{\hbar^2 k_0^2}{2m} \quad (2.3)$$

The condition for constructive interference in the reciprocal space can be determined by applying the law of momentum conservation:

$$\vec{k}_0 = \vec{k}' + \vec{g} \quad (2.4)$$

The Ewald sphere construction shown in figure 2.5 expresses the conservation of momentum from equation 2.4 in geometrical terms. Vector \vec{k}_0 with its tip pointing towards the origin of the reciprocal space, (000), represents the wavevector of the incident electron

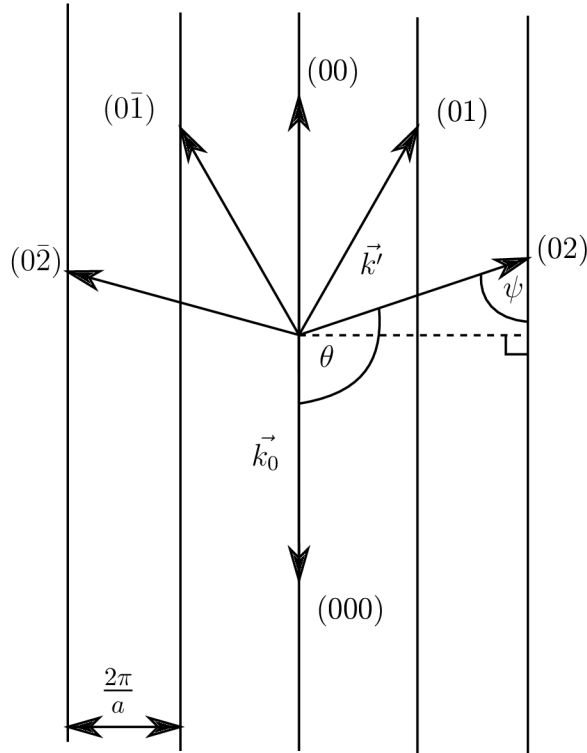


Figure 2.5: Ewald sphere construction. Schematic view in reciprocal space for an electron beam incident normal to the surface. Here \vec{k}_0 is the incident wave vector, \vec{k}' is the scattered wave vector, θ is the diffraction angle and ψ is the exit angle to the surface normal.

2. THIN FILM DEPOSITION AND CHARACTERIZATION

beam. A circle with radius $||\vec{k}_0||$, centred at the origin of the vector is a projection of the Ewald sphere. Its significance is that it maps the magnitude of \vec{k}_0 onto the reciprocal lattice – by conservation of momentum. No diffraction events can occur outside this sphere. If any of the reciprocal lattice “rods” are intersected by the Ewald sphere, then the elastic scattering condition from equation 2.4 is satisfied. This means that there is a change in momentum of the incident beam, but not its energy (equation 2.3). The scattered beam has a wavevector \vec{k}' . The points of intersection in the reciprocal space will then show as bright spots on the fluorescent screen of the LEED device.

The electrons in LEED have energies in the range 50 - 500 eV, which correspond to de-Broglie wavelengths of 0.5 - 2.7 Å. Such wavelengths correlate to atomic distances, hence the diffraction condition is satisfied in crystal lattice(s). The mean free path of electrons is only a few ML, therefore LEED is a highly surface-sensitive technique [10].

2.4. Magnetism

The ancients were acquainted with rather curious properties possessed by magnetic iron ore, which has the power of attracting iron [13]. This property of matter has later on been connected to electricity by H. Ch. Oersted in 1819 and finally a theory unifying electricity, magnetism and optics has been formulated to Maxwell equations in 1865 [14]. The purpose of this section is to point out the parts of this entangled world of electro-magnetism, which are necessary for understanding the basic principles of magnetism discussed in the experimental part of this thesis.

2.4.1. Categories of magnetic materials

Movement of a charge creates a magnetic field. Every atom has electrons that move around the nucleus and therefore induce magnetic field, so-called magnetic moment. Atoms with a magnetic moment in a material interact with each other. The exchange coupling describes how the electrons interact with each other and give rise to the bulk (or net) magnetism in a material. We distinguish diamagnetic, paramagnetic (non-magnetic), ferromagnetic and antiferromagnetic behaviour.

Diamagnetic materials have no net magnetization on their own. If they are placed in a magnetic field, however, the applied magnetic field affects the motion of the moving electrons. The electrons will produce a magnetic moment opposing that of the applied magnetic field. The orbital motion is electromagnetically induced by the applied magnetic field, as stated by the Lenz’s law - the induced current produces a magnetic flux that opposes any change in the applied field. This causes the material to be slightly repelled by the magnetic field.

The magnetic susceptibility $\chi = M/H$ quantifies the magnetic response M of a material to an external magnetic field H and is negative for diamagnetic materials, with the order of magnitude 10^{-5} .

Paramagnetism generally occurs in elements or compounds with unpaired electrons and have no net magnetic moment without applied magnetic field. The magnetization is proportional to the applied magnetic field and the magnetic susceptibility is therefore positive, with the order of magnitude between 10^{-3} and 10^{-5} . If the field is extremely

2.4. MAGNETISM

strong, however, the magnetic moments are oriented in the direction of applied field until maximum magnetization (*saturation*) is reached.

Ferromagnetism is a property exhibited by materials having long-range ordering which causes the spins of unpaired electron to line up parallel to each other in a region called the magnetic domain. Once a ferromagnetic (FM) material is magnetized, it will tend to stay in the magnetized state to some extent even after the removal of applied field. This characteristic is called *hysteresis*. The fraction of the *saturation* which is retained when the driving field is removed is called the *remanence* of the material, and is an important property of permanent magnets. The value of field required to reduce the magnetization to zero after reaching the saturation is called *coercive field* or *coercivity*. Ferromagnets have high magnetic susceptibilities ranging between 10^3 and 10^5 . The long range order abruptly disappears at a certain temperature which is called the *Curie temperature*. Above the Curie temperature, the thermal motion is sufficient to offset the aligning force, and the material becomes paramagnetic [15].

In materials that exhibit antiferromagnetism, the spins of magnetic electrons align in a regular pattern with neighbouring spins pointing in opposite directions; i.e. they have a negative coupling between adjacent moments. This is the opposite of ferromagnetism. Generally, antiferromagnetic (AFM) materials exhibit antiferromagnetism at low temperatures, and become disordered above a certain temperature; the transition temperature is called the Néel temperature. Above the Néel temperature, the material is typically paramagnetic.

2.4.2. Magnetic anisotropy

So far, we have considered the magnetic properties of homogeneous and isotropic materials. In reality, there are many factors which change properties of magnetic materials through introduction of anisotropies. For example, magnetic properties of a material depend on the direction in which they are measured. This dependence on the crystallographic directions is known as crystal (magneto-crystalline) anisotropy and is intrinsically associated with the crystal, whereas all other anisotropies (shape anisotropy, stress anisotropy etc.) are extrinsic or induced to the material. The crucial in creation of magnetic nanostructures in the Fe films on Cu will be the energetic difference between the crystal and shape anisotropies. For better understanding of the system studied in this thesis, we recommend referring to page 14 in [16].

2.4.3. Multi-layer systems

We have discussed magnetically homogeneous and anisotropic materials. Let us now look at a multi-layer systems, where the layers have different magnetic characteristics, are homogeneous, and the anisotropy of the system is therefore well-defined. An example of magnetic exchange across an interface is the exchange coupling across a FM/AFM interface: Let us imagine a system of a FM layer on top of an AFM one. If the case is that this system is inserted into a magnetic field, the ferromagnet will tend to adjust its spins in the direction of the field. The AFM layer, however, will have a very low magnetic response to this external field. The magnetic domains of the FM layer close to the AFM layer will therefore be submitted to two forces. One of them will be aligning them in the direction of the external field and the other one in the direction of the AFM layer.

For an oscillating external field, this behaviour will result in a hysteresis curve of an FM material shifted to side. This behaviour has been observed in [17], described at the end of the section 3.2.

2.5. Magneto-Optical Kerr Effect

Magneto-optics describe the effect of a magnetic surface on an electro-magnetic wave. In this thesis, we will focus only on the magneto-optical effects in solids. Michael Faraday discovered the first magneto-optic effect in 1845. He found that the effect of a magnetic field applied to a glass specimen was to rotate the polarization plane of transmitted light [7]. He subsequently experimented with light reflected from a metal surface in a magnetic field, but his results were inconclusive due to surface imperfections. Thirty-two years later (1877) John Kerr discovered this effect when examining the polarization of light reflected from a polished electromagnet pole [18].

The change of the electro-magnetic wave caused by the magnetic material is such that both rotation and ellipticity of the electric vector of a linearly polarized wave change. If the incident light is transmitted, these magneto-optical effects are called Faraday effect and if the light is reflected the Kerr effect; these two are pictured in figure 2.6(a). Both effects can be described by the complex angle, Φ_F or Φ_K respectively, which is proportional to the magnetization \vec{M} of the sample. This angle consists of two parts: the real θ , which expresses the direction of rotation, and imaginary ϵ which describes the ellipticity. Both variables are shown in figure 2.6(b). The change in rotation can be explained by the fact that the linearly polarized light can be divided into superposition of two circularly polarized light-waves (with an opposite direction). The coefficients of reflection for left and right polarized light are different in a magnetic material.

Because this work focuses on surface physics, we will use the Surface Magneto Optical Kerr Effect (SMOKE) for the study of magnetism of our samples [19]. SMOKE is a commonly used tool for the investigation of magnetic properties of a material and was extensively used in this thesis. Construction of the home-built setup used at the TU Wien is described in [20]. The main advantage of this setup is that it works in-situ and can therefore be used for magnetic characterization of samples without breaking the Ultra High Vacuum.

Light penetrates into metal more than 20 nm deep [19].

2.6. DEPOSITION OF THIN IRON FILMS

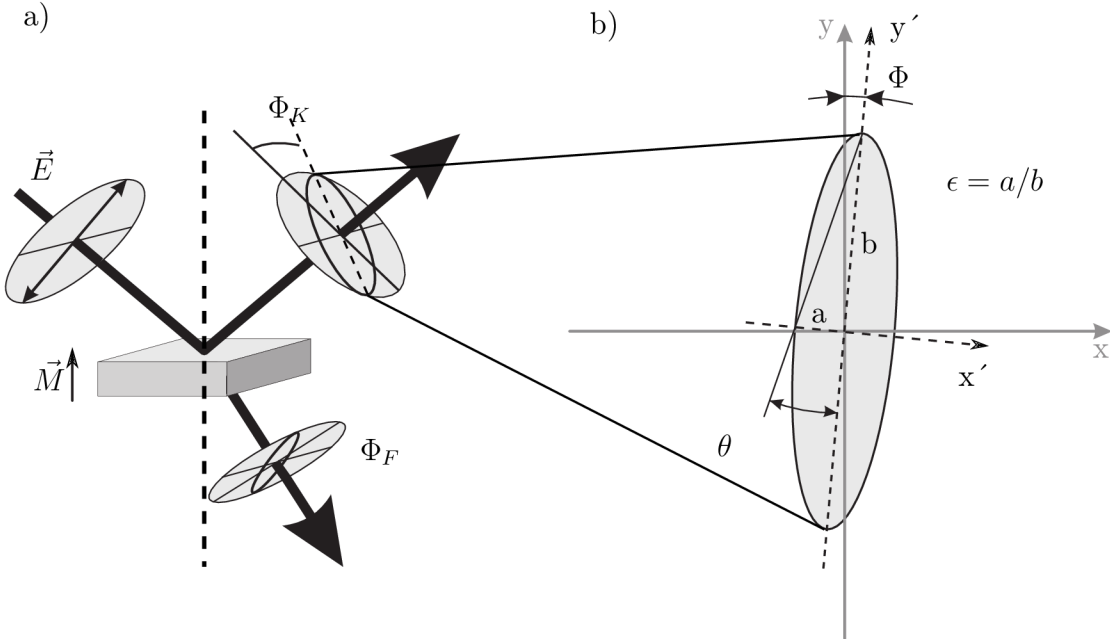


Figure 2.6: (a) Two main magneto-optical effects. The change of polarization of reflected light is called the Kerr effect and it is measured by SMOKE. If the light is transmitted, we name the process the Faraday effect. (b) Schematic view of the angle of rotation θ and the ellipticity ϵ , which define the complex number Φ of the Kerr effect. Adapted from [20].

2.6. Deposition of thin iron films

In 1967, it was found by Jesser and Matthews that metastable fcc Fe could grow epitaxially on Cu(100) [21]. The system Fe/Cu(100) was frequently investigated ever since. This review of the thin films of Fe/Cu(100) aims to give a fundamental understanding of the system to the reader. This will be necessary for the experimental part of this thesis.

2.6.1. Pure iron films

In the beginning of this chapter, the MBE and the heteroepitaxial systems have been described. Fe grows on Cu in the layer-by-layer regime, in which we distinguish three distinct epitaxial regimes. The reason for this is that in heteroepitaxy the lattice parameters of the film and substrate are necessarily unmatched, and, depending on the extent of the mismatch, we distinguish matched, strained and relaxed epitaxial regimes [8].

The bulk Fe exists in the α phase and has a body-centered cubic (bcc) crystallographic structure, which is ferromagnetic at room temperature (RT). Above the Curie temperature (T_C), it attains the γ phase [face-centered cubic (fcc), non-magnetic]. Table 2.1 includes some basic properties of Fe and Cu. The lattice constant difference between bcc Fe and fcc Cu is 0.749 Å. On the other hand, if we extrapolate the lattice constant of γ phase fcc Fe to RT, we find that the lattice constant is in the range of 3.55 - 3.58 Å [22]. When compared to the Cu, the lattice constant difference is ~ 0.05 Å, which is much lower than that of bcc Fe.

2. THIN FILM DEPOSITION AND CHARACTERIZATION

It can therefore be expected that the growth of Fe on Cu(100) will be directed by two main energy constraints. One of them will be the energy gain of the pseudomorphic growth and the other the energy advantage of the α phase bcc bulk Fe. The result of these competing energies are the three thickness regions portrayed in figure 2.7 and a potential energy curve further discussed in figure 2.9(b). The first region below 5 ML is the growth of bcc strained Fe with out-of-plane magnetic moments (red arrows), which is ferromagnetic. Once the film thickness grows over the 5 ML, the film grows as γ -fcc and is paramagnetic. The fcc phase of the Fe film relaxes, although a few thin and prolonged bcc domains (so-called bcc needles) can be observed. These bcc needles have been analyzed by Biedermann et al. [1] and are depicted in figure 2.8. The STM image on the left confirms the layer-by-layer growth (described in section 2.1) of the as-deposited 7 ML thick Fe film on Cu(100) and the bcc needles are marked with arrows. One of the needles has been analysed by STM on an atomic level, as shown in figure 2.8. This shows the difference between the fcc(100) and bcc(110) composition. The crystallographic planes are shown by orange rectangles. We can observe that the result of a change from fcc(100) to bcc(110) is that (i) the atomic distance increases and (ii) the unit cell tilts by 15° . This behaviour has been analysed in reference [1] with the outcome that the bcc needle is strained. This strain leads to a structural (and magnetic) phase change in case that the film grows even further.

Table 2.1: A Comparison of Physical Properties of Iron and Copper

Property	Cu	Fe
Crystallographic structure at RT	fcc	bcc
Lattice constant	3.615Å	2.866Å
Atomic number	29	26
Atomic radius	1.28Å	1.27Å
Melting temperature	1083K	1808K

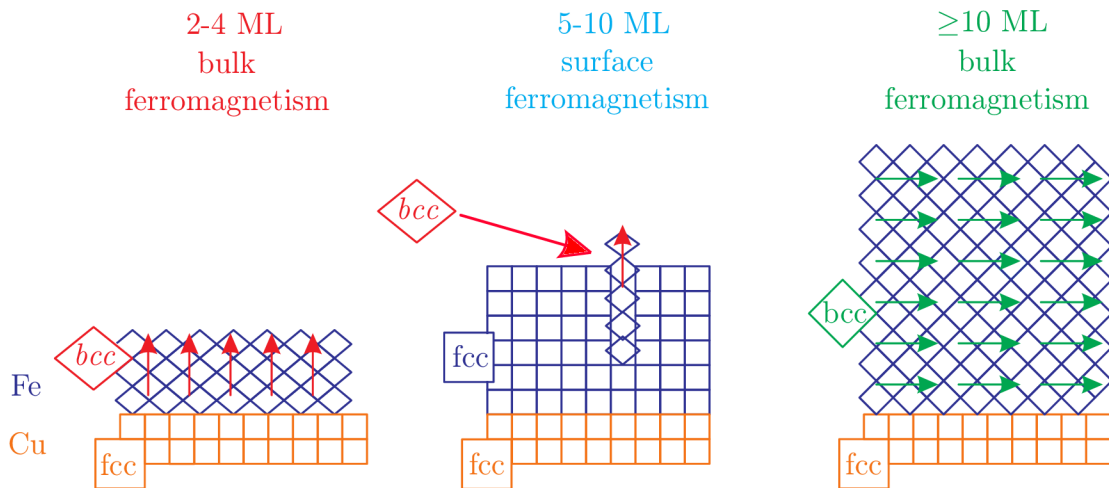


Figure 2.7: Three growth regions of Fe/Cu(100), showing a strong dependence of the magnetic moments on the thickness of the film. Adapted from [16].

2.6. DEPOSITION OF THIN IRON FILMS

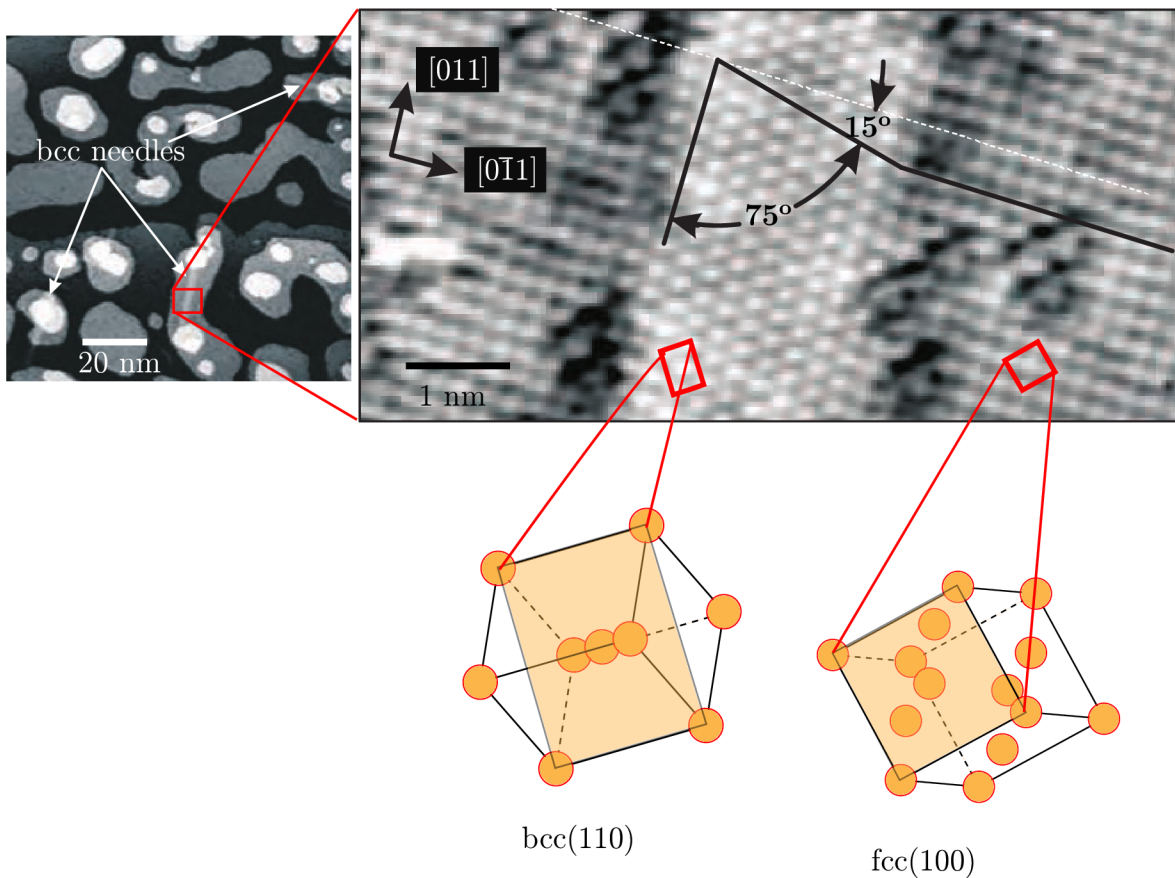


Figure 2.8: STM image of a 7 ML thick Fe film on Cu(100) and an analysis of a bcc needle. The analysis shows the difference in atomic structure between the fcc and bcc areas on the film. Adapted from [1].

Above 10 ML, the gain in structural energy of the α bcc phase overrides the energy gain of the epitaxial growth on Cu(100) and the film grows in relaxed form. From the point of view of magnetism it becomes ferromagnetic again, this time with in-plane magnetic moments (green arrows), as shown in figure 2.7.

2.6.2. Ion beam irradiation of pure iron films

In 2008, Werner Rupp et al. [2] demonstrated that Ar ion irradiation can be used to induce structural change from fcc γ phase to bcc α phase in a 8 ML thick Fe film epitaxially grown on a Cu(100) single crystal. The significance of this model in comparison to other currently investigated systems [23] is that the material is non-magnetic prior irradiation. Transformation from a non-magnetic to a ferromagnetic state is interesting for practice, since it makes it possible to write arbitrary magnetic patterns that are magnetically isolated by non-magnetic regions. This will be described in the review in section 3.3.

We already discussed that it is energetically more favourable for the film to grow in the fcc state in case that its thickness is between 5 and 10 ML. Figure 2.9(b) describes the energetic barrier that is overcome by the strain at the 10 ML boundary. From the curve simulated by Entel et al. [24], it is clear that the Fe film is metastable in the

2. THIN FILM DEPOSITION AND CHARACTERIZATION

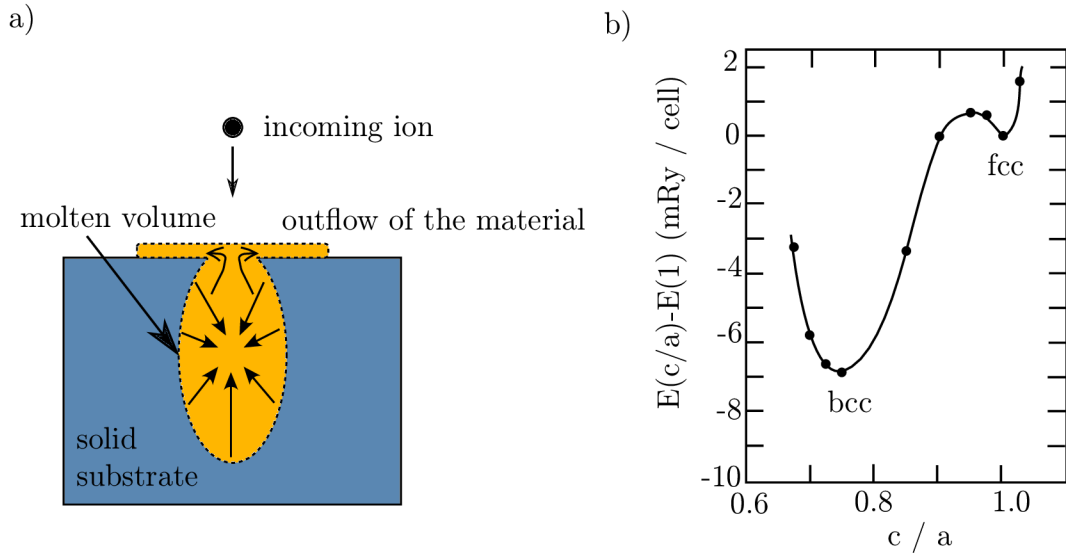


Figure 2.9: (a) The thermal-spike model. An incident ion transfers its energy during the collision to an atom and a volume in the substrate around the atom melts. Some of the molten volume floats out of the substrate. The molten volume freezes within picoseconds. Adapted from [16]. (b) Results of total-energy calculations for Fe_3Ni from the fcc to the bcc structure. The energy difference between the two structures is of the order of 1.5 (mRy)/atom. Note that the volume of the bcc structure ($c=2.67$) is larger than the fcc structure ($a=2.60$ a.u.). Adapted from [24].

fcc phase and in the event that the atoms obtain extra energy to overcome this barrier by an incident ion, it will be possible to change its crystallographic structure. Scanning Tunneling Microscopy (STM), LEED and SMOKE have been used for an analysis of the film, showing the effect of an ion-beam-induced structural change. At first, the nucleation of bcc needles was observed. The final result of the irradiation was that the Fe film became strongly ferromagnetic at room temperature. The reason for the structural change due to ion beam irradiation is explained by the Thermal spike model.

Thermal Spike Model

Let us now describe the behaviour of a substrate in case that it is hit by an ion [figure 2.9(a)]. Energy of an ion spreads homogeneously over a small volume in the substrate. This volume is consequently molten within picoseconds. Because the volume has a smaller density, some of the atoms in the molten volume float out of the volume on top of the substrate. The molten volume then freezes out. It proved to be extremely important that the molten volume could freeze in a different phase compared to its surroundings. However, the probability of this happening is very low [25].

2.6.3. Growth of iron films in carbon monoxide

Using the properties of Fe films on Cu(100) for application, it is desirable to grow thicker films. Kirilyuk et al. [26] published in 1996 that γ Fe films up to 50 ML can be grown epitaxially on Cu(100) in the event that they are for instance deposited in a carbon monoxide (CO) atmosphere. The mechanism of this system is described by figure 2.10:

2.6. DEPOSITION OF THIN IRON FILMS

A CO molecule arrives at the surface of an already-deposited Fe film and dissociates on it. The carbon is then incorporated into the growing Fe film, remains in the bulk and supports the metastable γ phase fcc Fe. Oxygen, on the other hand, remains on the surface and helps the layer-by-layer growth as a surfactant. The effect of the CO therefore is that it supplies the interstitial C and surfactant O to support the growth of the γ phase fcc Fe. The limiting factor of this system is that the O will eventually saturate the surface with its $c(2 \times 2)$ superstructure, which prohibits further CO dissociation. If there is no more CO dissociation, C will not go into the bulk and the phase transformation will take place. Kirilyuk et al. [26] has proposed that the saturation of the surface by O occurs at a maximum thickness of ~ 50 ML thickness of Fe, confirmed by Reflecting High Energy Electron Diffraction. Shah Zaman et al. [4] have shown, however, that the effect of the CO allows to move the phase change occurring at 10 ML described in section 2.6.1 only to 22 ML, confirmed by LEED, SMOKE and STM.

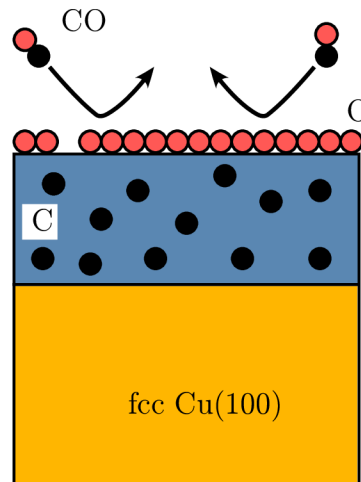


Figure 2.10: Schematic view of the proposed CO dissociation mechanism, adapted from [16]. A CO molecule arrives at the surface, dissociates and C is incorporated into bulk, whereas O floats on the surface.

2.6.4. Growth of alloys of iron with nickel

Due to the problem with incorporation of C into the thicker film, there was a search for another stabilizing agent. Alloying with Nickel was chosen as a substitute for interstitial C. The reasons for this were that Ni is ferromagnetic, it is stable in fcc phase at room temperature and has the lattice parameter and atom diameter comparable to Fe, as shown in table 2.2. This makes it an ideal candidate for alloying with Fe. A phase diagram of Fe and Ni in figure 2.11 describes the crystallographic and magnetic behaviour of an Fe-Ni alloy.

Let us look at the phase diagram in more detail. In the event that the alloy has more than 90% of Fe, it is bcc ferromagnetic (left), as shown by the magnetic moment line and discussed previously in section 2.6.1. If, on the other side of the figure, the alloy has less than 50% of Ni, a sharp decrease of the Curie temperature in the region down to 30% of Ni can be observed, alongside with a decrease of the net magnetic moment. This can be attributed to a less organized structure due to the difference in relaxed

2. THIN FILM DEPOSITION AND CHARACTERIZATION

crystallographic structures of Fe (bcc) and Ni (fcc), which becomes more pronounced as their ratios approach the boundary marked by the dashed line. At the boundary of approximately 25%, a phase change (from fcc to bcc) of the alloy occurs. The alloy is therefore extremely sensitive to any external factors, if grown with this ratio of Ni and Fe. This external factor could be, for example, an incident ion. For this reason, the metastable thin films of $\text{Fe}_x\text{Ni}_{1-x}$ on Cu(100) started to be investigated at the TU Wien in 2010 [16].

In order to find the appropriate Ni concentration to grow the metastable γ Fe, Shah Zaman deposited $\text{Fe}_x\text{Ni}_{1-x}/\text{Cu}(100)$ films with Ni concentrations varying from 13% to 22%. The structural analysis was performed in a home-built Scanning Tunneling Microscope (STM) at the TU Wien. The STM images of the film with a Ni concentration of 13% revealed that most of the film is spontaneously transformed to bcc (α phase), with very few remaining untransformed regions [figure 2.12(a)]. The areas spontaneously transformed to bcc exhibit wavy ridges with a typical spacing of 10–20 nm and lengths

Table 2.2: A Comparison of Physical Properties of Iron and Nickel

Property	Ni	Fe
Crystallographic structure at RT	fcc	bcc
Lattice constant	3.52Å	2.866Å
Atomic number	28	26
Atomic radius	1.24Å	1.27Å
Melting temperature	1728K	1808K

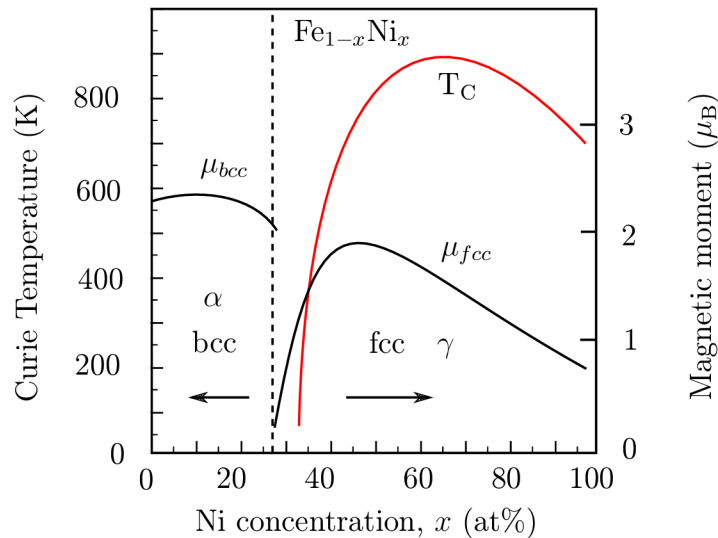


Figure 2.11: Magnetic and structural phase diagram of $\text{Fe}_x\text{Ni}_{1-x}$. Curie temperatures in the γ phase and the magnetic moment in the α bcc and γ fcc phase are given as function of the Ni concentration. Note that the region of structural bcc \rightarrow fcc transformation is around 23% of Ni. Adapted from [15].

2.6. DEPOSITION OF THIN IRON FILMS

up to several hundreds of nanometers. An analysis of the surface [inset in figure 2.12(a)] elucidated that the corrugation is about 1.5 nm. Reason for the corrugation is the difference between the interlayer distances of bcc(110) Fe (0.20 nm) and fcc(100) Fe (0.18 nm) [1].

When the Ni concentration was increased to 15%, STM exhibited an untransformed fcc γ Fe surface with a few bcc needles [figure 2.12(b)]. The inset of the image reveals monatomic steps and nearly perfect layer-by-layer growth, resembling a typical 8 ML fcc Fe film surface [2]. After ion irradiation with a dose of $2 \times 10^{14} \text{ cm}^{-2}$, the film is partially transformed to bcc [figure 2.12(c)]. Transformed areas are bright and rougher than the fcc regions; they form narrow needles oriented along the close-packed directions of the fcc substrate as well as large patches. The film is completely transformed to bcc after irradiation with a dose of $3 \times 10^{15} \text{ cm}^{-2}$ [figure 2.12(d)].

Further increase of the Ni concentration to 21% leads to a non-transformable films with a stable fcc γ phase. The surface of the as grown film demonstrates layer-by-layer growth, with no bcc areas [figure 2.12(e)] and figure 2.12(f) indicates that no bcc areas appear even after a prolonged irradiation.

Shah Zaman was successful in stabilizing a thicker fcc Fe film, which was 44 ML thick by alloying with Ni. She claims, however, that it was difficult to reproduce due to its dependence on the rates of evaporation of Fe and Invar evaporators. She found that the fcc Fe film can be stabilized if the Ni concentration is close to $\sim 15\%$. When the concentration is lower, the films is already transformed into the bcc phase after the deposition and in case that the the concentration is higher, the film grows as stable fcc. She also observed transformation from fcc Fe to bcc Fe by Ar irradiation at 2 keV by STM.

2. THIN FILM DEPOSITION AND CHARACTERIZATION

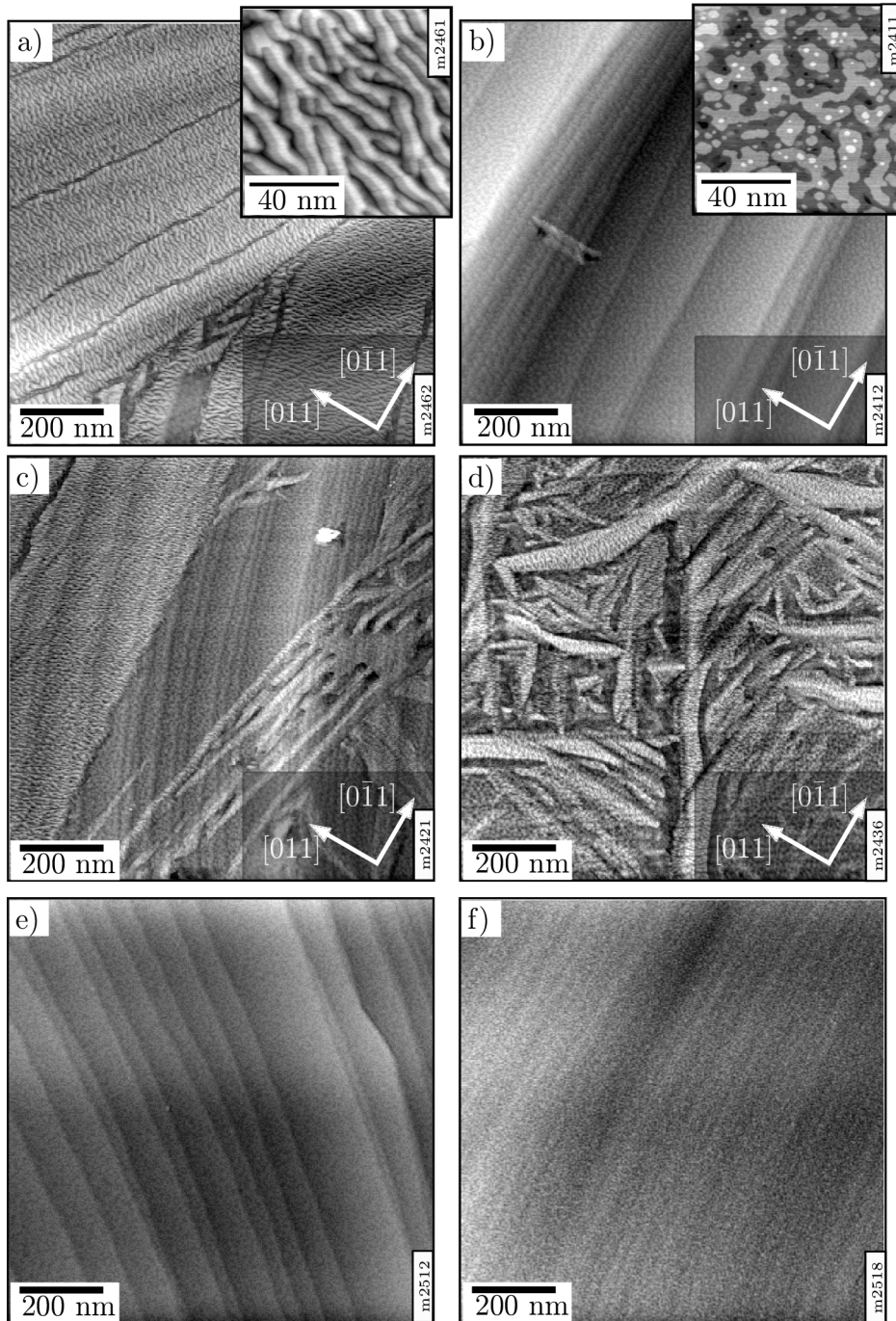


Figure 2.12: STM images of as-deposited 44 ML fcc Fe films with Ni concentrations of (a) 13%,(b-d) 15% and (e-f) 21%. The film shown in (b) was transformed by 2 keV Ar ions with a dose of (c) $2 \times 10^{14} \text{ cm}^{-2}$ and (d) $3 \times 10^{15} \text{ cm}^{-2}$. Areas transformed to bcc appear brighter (higher) and rough due to narrowly spaced ridges [inset in (a)]. (e) is an image of as deposited film, which could not have been transformed even after prolonged irradiation (f). Adapted from [6].

3. Patterning and characterization of magnetic nanostructures

Manufacturing of magnetic nanostructures by means of ion-beam irradiation has been first published in 1998 [27] and thoroughly investigated ever since. The main advantage of this approach over e.g. lithography is that the patterning is purely magnetic, i.e. non-topographic. No topographic signal in measurements of magnetic domains results in higher signal-to-noise ratio, what then in turn allows a decrease in size of the domains.

Let us now describe the methods that followed after the publication of Chappert et al. The short review will be divided into three sections. The first section will discuss the theoretical background and techniques important to understanding the concepts described in the review itself. Second section will focus on the irradiation and implantation effects in ferromagnetic films. These modifications would usually lead to a decrease of magnetization in the layers. In this section we will focus on the origin of these magnetic modifications. The variation in magnetism of thin films originates from structural modifications of either the interface structure, the atomic short range order, the crystalline phase, the degree of ordering or the composition of the material due to ion irradiation and/or implantation. The third section will deal with the creation of magnetism in non-magnetic thin films due to the ion-beam irradiation. This section will be concluded with description of nanopatterning of the system, which was the predecessor to the one we have investigated. The main resource of this review (i.e. sections two and three) was the work of Fassbender and McCord [23].

3.1. Theoretical background and techniques

There is a wide range of techniques for patterning and characterization of structures at nanoscale. Considering nano-patterning, we will limit ourselves to Focused Ion Beam (FIB), because this method allows us to write finely defined patterns, considering ion dose, beam dwell time, spot size etc. To characterize nanostructures created by FIB, we have used Atomic and Magnetic Force Microscopies (AFM and MFM, respectively) and Scanning Electron Microscopy (SEM). Especially the latter offers an extremely powerful tool for nanopatterning and nanofabrication in case that it is combined with FIB, as was in our case.

3.1.1. Atomic and Magnetic Force Microscopies

The Atomic Force Microscopy (AFM) was introduced in the 1986 by Binnig et al. [28]. The AFM studies the surface of the sample by measuring the mutual force interactions between the atoms of a very sharp apex and the sample surface atoms. Forces measured by AFM include mechanical contact force, chemical bonding, electrostatic forces, magnetic forces etc. A schematic diagram of an AFM microscope is shown in figure 3.1(a). Cantilever is the part of the AFM that is in direct contact with the surface. The tip is either of a conical or a pyramidal shape and together with the cantilever it is typically made of highly doped silicon to avoid charging and allow combination of tunnelling and force microscopy experiments [29]. Important parameters of the tip are its apex radius

3. PATTERNING AND CHARACTERIZATION OF MAGNETIC NANOSTRUCTURES

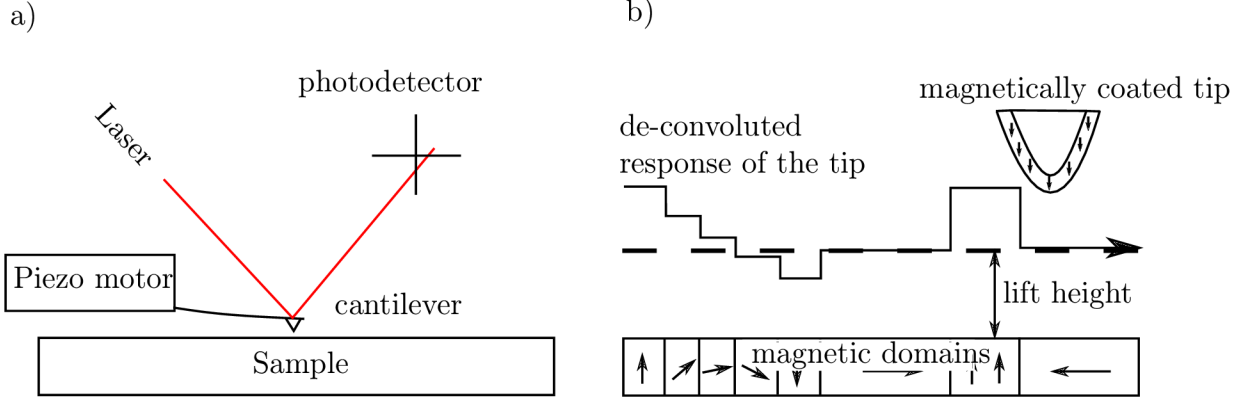


Figure 3.1: (a) Scheme of an AFM microscope with moving sample and an oscillating tip. The topography is measured from the change of the laser light signal on the quadrupole. (b) A detailed view of a coated MFM tip which interacts with magnetic domains on a sample.

and the top angle. The tip is attached to a cantilever arm. The cantilever arm is usually rectangular, or of an A letter shape, and the top of the arm is covered by reflecting layer. This arm is integrated into a rectangular girder. A cantilever is defined through its dimensions s, t, v [μm], spring constant k [Nm^{-1}] and a resonant frequency f_0 . The tips used for measurements in this thesis were from the company Nanosensors had the resonant frequency in the range from 60 to 90 kHz.

Piezoelectric crystals are used for the movement of the tip on the sample, when either the tip and/or the sample is moved. The resulting map of the area $z = f(x, y)$ represents the topography of the sample. The AFM can be operated in a number of modes, depending on the application. In general, possible imaging modes are divided into static (also called contact) modes and a variety of dynamic (non-contact or "tapping") modes. In the case of the non-contact mode, we further distinguish a constant height and a constant force mode. In the case of the constant height mode, the deflection of the cantilever is measured according to the forces exerted on it. During a constant force mode a feedback mechanism is employed to adjust the tip-to-sample distance to maintain a constant force between them.

The basic principle of MFM is that a magnetic probe reacts to the magnetic field created by the sample. The interaction with the external field causes a phase change in the vibrations of the probe. The response of a MFM probe [figure 3.1(b)] to magnetic signal coming from the sample is recorded at some distance from the sample, the *lift height*. The reason for this is that the response of the tip to the topography decreases by the order of r^{-7} and the magnetic forces decrease only by the factor of r^{-2} . The MFM measurement therefore consists of two steps: first, the topography of the sample is measured and second, the tip is lifted to the lift height and runs over the surface in the constant height mode. The resulting signal then gives information about the magnetic properties of the sample.

3.2. MAGNETIC NANOSTRUCTURES IN MAGNETIC FILMS

3.1.2. Focused Ion Beam and Scanning Electron Microscopy

Focused Ion Beam (FIB) is an extremely useful tool for laterally well-specified irradiation of materials by ions. The examples of its use are preparation of samples for the Transmission Electron Microscopy (TEM), manufacturing nano-sized elements, imaging of the surface via either scattered ions or secondary electrons, etc. [30]. The FIB direct writing can combine a series of techniques such as milling, implantation, ion-induced deposition, ion-assisted etching and energy transfer associated with structural (phase) change. The performance of a modern FIB setup allows one to mill nanostructures with the ultimate resolution of approximately 10 nm at a reasonable speed: a 30 nm thick permalloy thin film can be removed at a rate of $10 \mu\text{m}^2 \text{min}^{-1}$ at the highest resolution [31]. An example of degradation of magnetic properties by a complete removal of the magnetic material is shown in figure 3.2.

In our investigation, we will be using FIB with Ga ions. When 30 keV Ga ions hit the surface of a film, they penetrate into a depth of approximately 5–40 nm, depending on the material. On their way through the film, the ions lose their energy due to interactions with target atoms and form collision cascades [32]. The collisions between the ion and the atoms is described on the base of a thermal spike model, discussed in section 2.6.2.

SEM uses electrons for imaging of the surface. It can be considered a substitute for the optical microscopy on the nanoscale range. The reason for this is that the electrons have significantly lower wavelength compared to photons, and can thus show structures at the nanoscale without limiting constraints arising from diffraction described by the Rayleigh criterion. The experiments in this thesis have been done with the LYRA FIB/SEM machine from the company TESCAN.

3.2. Magnetic nanostructures in magnetic films

As already mentioned in the section 2.4.1, the exchange coupling is the factor responsible for magnetization of a material. We will distinguish two main characteristics which affect the exchange coupling.

First are the short-range order effects in amorphous alloys or chemically ordered crystallographic structures. Through quantum mechanical overlap of the wave functions, these ferromagnetic constituents govern the overall magnetic behaviour. In the event that the structures, with such short-range order effects are irradiated, the irradiation destroys the order along with the magnetism.

The second characteristic is that the film (an alloy or a multilayer system) grows in a disordered phase, which gets ordered with the mixing of the layers. This then gives rise to the exchange coupling.

Let us now look closely to the first characteristic. An extreme example is, as already mentioned in section 3.1.2, the ion irradiation used for complete removal of the ferromagnetic layer in selected areas (figure 3.2) [31]. The FIB irradiation was in this case used for milling of the permalloy. A complete removal of the film led to confinement of the magnetic moment into rectangles. This method, however, leads to creation of a height profile, which has the height of the deposited film.

A different approach, which changes the short range order effect is the implantation of atoms - conventional doping can, for example, be employed to modify the Curie temperature of a ferromagnetic material. In addition, it has been recently demonstrated that

3. PATTERNING AND CHARACTERIZATION OF MAGNETIC NANOSTRUCTURES

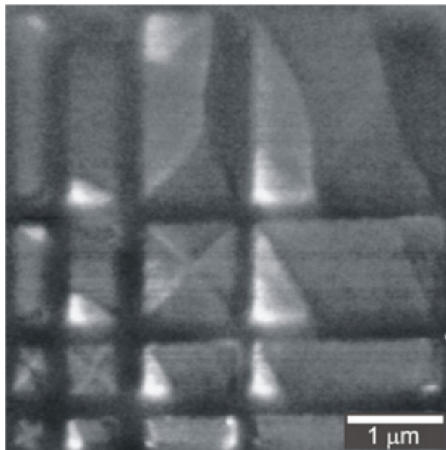


Figure 3.2: MFM image of spintronic nanostructures fabricated by FIB milling of a permalloy film. In some of the squares the magnetic moments align to form Landau patterns. Most of the other structures have near-single domain S or C-states [31].

the magnetic damping behaviour can be effectively tailored by doping transition metals into the ferromagnetic films. By these means, an optimized magnetization-switching behaviour could be achieved [33].

Fassbender et al. [34] have also shown that ion beam mixing of metal interfaces can lead to a structural phase transformation from a crystalline to an amorphous phase. The origin of this effect is the doping of an interface near region above a critical threshold value which is required for irradiation induced amorphization.

Let us discuss the main result of [34]. In figure 3.3, cross-sectional TEM images for the as deposited sample (left) as well as for two different Ni implantation fluences are presented. For the as deposited sample the interface between the $\text{Ni}_{81}\text{Fe}_{19}$ film and the Ta buffer layer is well resolved due to the mass contrast. The single crystalline nature of the $\text{Ni}_{81}\text{Fe}_{19}$ grain is proven by the appearance of atomic rows. The thickness of the individual layers is determined to be 17.5 nm and 5.2 nm, respectively. For increasing implantation fluences the thickness of the bilayer stack, i.e. the sum of the $\text{Ni}_{81}\text{Fe}_{19}$ film and the Ta buffer layer is reduced from 22.7 nm (as-deposited) to 22.2 nm due to sputtering effects. In addition, the mass contrast at the interface between the Ta layer and the $\text{Ni}_{81}\text{Fe}_{19}$ film gets weaker. However, with increasing implantation fluence, the signature of an amorphized region is becoming more pronounced. Thus, the position of the interface is defined by the transition from an amorphous to a crystalline region. This position is shifted closer to the sample surface as expected from simulations. For implantation fluences above 1.2×10^{16} Ni/cm², the continuous crystalline $\text{Ni}_{81}\text{Fe}_{19}$ film breaks up and only crystalline particles are left within an amorphous matrix impeding a similar analysis for higher ion fluences.

In 2010, Martin-Gonzales et al. [35] reported that their technique could be a feasible industrial production method for nano-patterning hard disk magnetic media with perpendicular magnetization, while preserving surface flatness. The base principle was that low energy chemically reactive ion implantation modifies the structural and the magnetic properties of magnetic multilayers with perpendicular anisotropy (e.g. Co/Pd multilay-

3.2. MAGNETIC NANOSTRUCTURES IN MAGNETIC FILMS

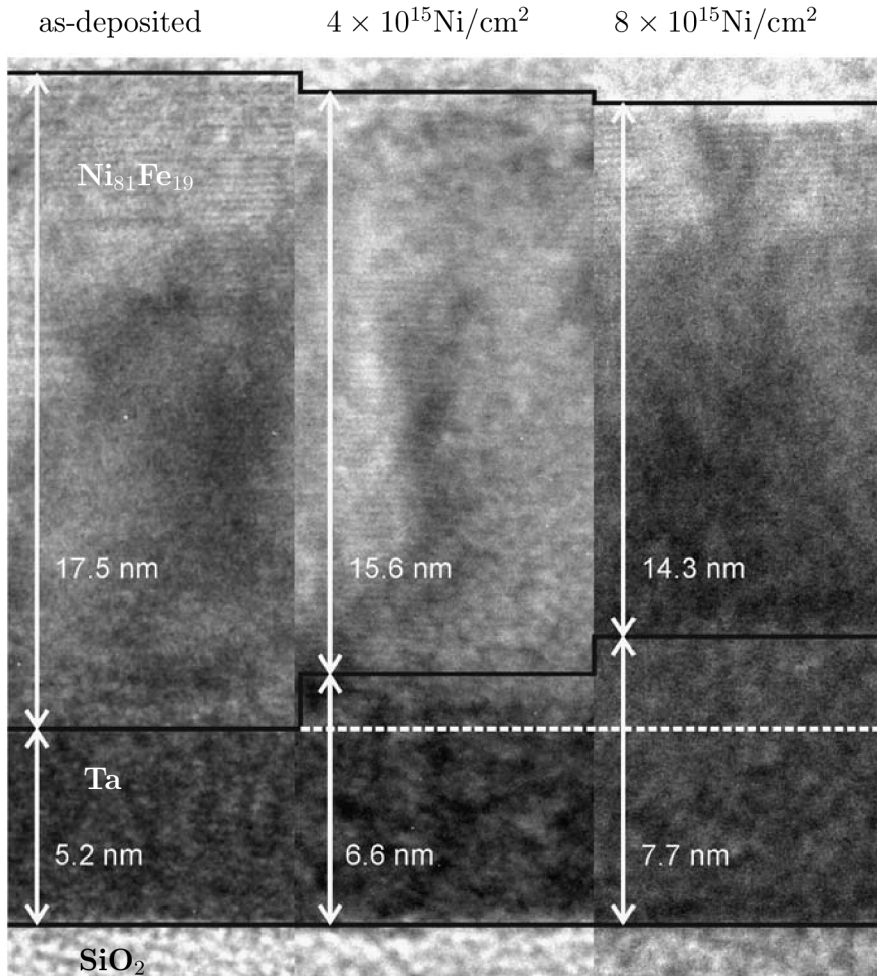


Figure 3.3: Cross-sectional TEM images for as-deposited and irradiated Ni₈₁Fe₁₉/Ta and Ta/SiO₂. The boundaries are indicated by black lines. The white dashed line encloses the amorphized region. Adapted from [34].

ers). In the system they have studied, an interfacial disorder was generated for N ions. This gave rise to a strong reduction of the local magnetic anisotropy and exchange coupling. A stronger reduction was observed for P and As ions when a chemical bonding with Co was established. Heavier ions like P were a better choice for damage depth optimization, polymer mask thickness reduction and lateral ion straggling limitation. In this paper, it was proposed that by using proper masks and flux densities, magnetic recording media with perpendicular anisotropy and magnetically hard bits arranged into a non-magnetic matrix can be fabricated.

As already mentioned, the exchange coupling can be tailored in multilayer systems, which grow with a disordered phase. In case that these layers are irradiated, the exchange coupling arises along with the ordering of this phase. It was published [36] that light ion irradiation of the initially disordered Fe₅₀Pt₅₀ alloy can significantly enhance the degree of L1₀-ordering. The reason for this is that the chemically ordered L1₀-phase is thermodynamically favoured.

3. PATTERNING AND CHARACTERIZATION OF MAGNETIC NANOSTRUCTURES

The ion beam induced modification of the exchange coupling across an antiferromagnetic/ferromagnetic interface is widely investigated for exchange bias systems. These for example include spin-valves and magnetic tunnel junctions. In all these situations the magnitude of the exchange bias effect is directly related to the exchange coupling across the mutual interface between the ferromagnet and the antiferromagnet. Because an intermixing of the interface occurs upon ion irradiation, this exchange coupling is usually weakened and thereby the exchange bias effect is reduced. Spintronic structures are usually prepared by sputtering deposition of layered structures. The layers consist of magnetic and non-magnetic metallic or dielectric thin films with the thickness typically in the range of 5–50 nm [37].

Blomeier et al. [17] demonstrated that antiferromagnetically coupled Fe/Cr/Fe trilayers can be magnetically patterned on the micrometer and sub-micrometer scale by irradiation with Ga ions with energy of the order of keV. These ions induced a local transition to ferromagnetic coupling due to direct contact between the two Fe layers via ferromagnetic pinholes. The irradiated areas acted as ferromagnetic elements which were embedded into a surrounding, antiferromagnetically coupled trilayer. They also demonstrated that the magnetic properties of the elements fabricated by this method were size dependent, including a transition from multi-domain to single-domain configurations with decreasing element size. Finally, they determined an effective intrinsic limit to the lateral resolution of this patterning technique.

3.3. Magnetic nanostructures in non-magnetic films

For all examples previously described in this short review, the irradiation or implantation modified the magnetic parameters of a ferromagnetic film or multilayer structure. Let us now consider materials which are paramagnetic prior irradiation. The transformation from a non-magnetic to a ferromagnetic state is most desirable for applications, making it possible to write arbitrary magnetic patterns that are magnetically “isolated” by non-magnetic regions.

For example, the crystallographic structure of an Fe₆₀Al₄₀ alloy is the chemically ordered B₂-phase [38]. After the ion irradiation the phase is transformed to the chemically disordered bcc phase, which is ferromagnetic. Due to the local irradiation, ferromagnetic nanostructures can easily be created in such paramagnetic environment.

Similar behaviour has been reported for the chemically ordered alloys such as PtCo [39, 40] (figure 3.4) or FePt₃ [41]. The chemical ordering in the material was reduced by ion bombardment, which led to a change in the coercivity, the easy axis of magnetization, and the magnetization itself. Using ion-beam induced chemical disordering for this purpose requires sufficiently low Fe or Co content for the material to be non-magnetic in the chemically ordered form. Therefore, these materials tend to have low Curie temperatures and relatively low magnetization values by design.

In figure 3.5(b) a different approach is demonstrated. It has been published [2], that it is possible to pattern alloys with much higher Fe content by an ion-beam induced change in the crystallographic structure, from paramagnetic fcc (γ -Fe) to ferromagnetic bcc (α -Fe) as already discussed in section 2.6.2. In this model system, pure Fe was evaporated on a Cu(100) single crystal at room temperature. As already mentioned in section 2.6.1 films between 5 and 10 ML thick adopt the fcc structure of the substrate, even though

3.3. MAGNETIC NANOSTRUCTURES IN NON-MAGNETIC FILMS

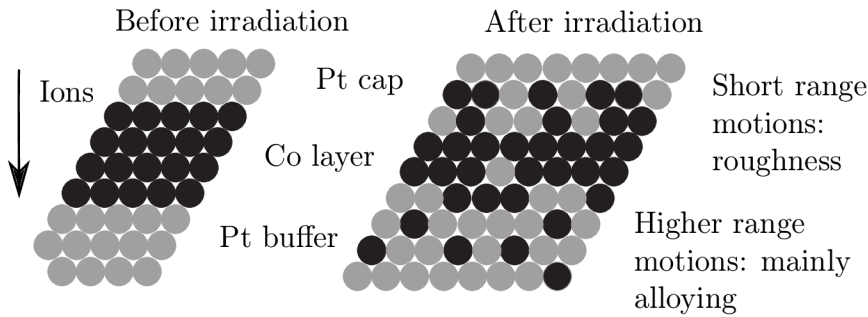


Figure 3.4: Sketch of the irradiation induced intermixing at the upper and lower Co/Pt interface. In this system, the strong perpendicular magnetic anisotropy is an interface anisotropy, which originates from the atomically sharp interfaces between the individual layers. A broadening of the interfaces immediately leads to a reduction of this anisotropy contribution and the saturation magnetization. Adapted from [40].

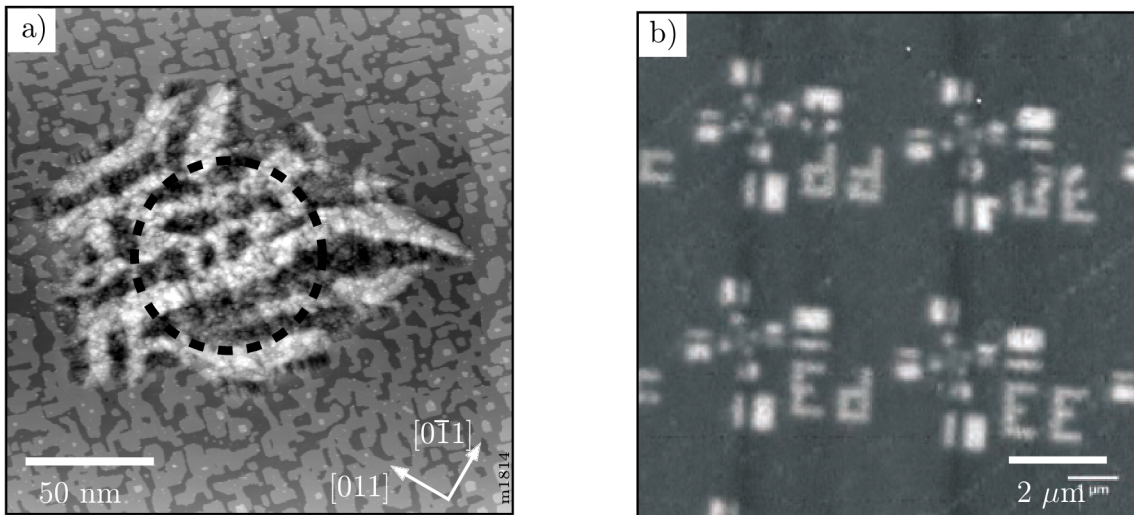


Figure 3.5: (a) STM image of a nano-dot in a 22 ML thin film made through a mask [3]. (b) Nanopatterning of 8 ML thin film through a lithographically made mask [2].

the stable bulk structure of Fe is bcc. The occurrence of rare bcc nuclei shows that the fcc structure is only metastable with respect to transformation into bcc.

As was already mentioned in section 2.6.3, the limit for the metastability of the pure Fe films is 10-ML. In order to grow thicker films, which are important for applications, it was necessary to increase the thickness of the film by deposition in a CO atmosphere. Figure 3.5(a) shows a nanodot made in a 22-ML Fe film, which was deposited in the CO atmosphere [3].

The last figure (3.5) concludes the review of magnetic nanostructures fabrication. It also was a starting point for investigation of micro- and nanostructures in thicker films of Fe alloyed with Ni.

4. Deposition of thin Fe_xNi_{1-x}/Cu films

The experiments discussed in this chapter were commenced in 2012 at the TU Wien. Author's Erasmus stay at the TU Wien in 2013 offered a great opportunity to continue with this research. The purpose of our investigation was to move the experiments performed by Shah Zaman to a different Ultra High Vacuum (UHV) system, which would allow measurement of magnetic characteristics. The experiments performed by Shah Zaman were already discussed in section 2.6.4 and gave a sound starting point for the investigation.

We have continued with the research of the $Fe_xNi_{1-x}/Cu(100)$ in a different UHV system equipped with a Surface Magneto-Optical Kerr Effect (SMOKE) apparatus, that allowed us to measure the magnetic properties of deposited films. This system will therefore be referred to as the SMOKE system. Majority of the experiments has been performed in the SMOKE chamber at the TU Wien. This chamber is equipped with a triple Omicron EFM3-T and a single Omicron EFM3 evaporators for thin-film deposition and facilities required for moving and storing of samples. Samples were irradiated by a Leybiq ion gun (sputter-cleaning of the sample) and a Specs IQE 12/38 Ion Source with a Wien filter. The latter has been used for transformation of the sample because of its high scanning and focus precision. The techniques used for thin film characterization were except SMOKE also LEED and AES. The chamber was also equipped with a cryo baffle and a Titanium Sublimation Pump.

4.1. Sample Preparation

In order to have a well-focused ion beam on the sample, its position with respect to the Specs ion gun has been optimized. For this, the ion gun (x-y scanning) and an amperemeter connected to the manipulator (intensity) have been attached to an oscilloscope. Different materials have different probability of ionization and in this way the position of the crystal has been resolved. The Leybiq ion gun has been optimized in a similar manner, but only roughly due to its high ion flux and no necessity for precise flux control on the sample. Figure 4.1 shows a capture of the sample plate made of Mo with a Cu(100) single-crystal, as seen in ambient conditions (a) and in the oscilloscope during scanning with the Specs ion gun (b).

4.2. Deposition

Prior the deposition, the Cu(100) single-crystal has been cleaned by sputter-anneal cycles. One cycle consisted of sputtering for 40 minutes by an Ar ion beam with energy of 2 keV and annealing to 520°C for 10 minutes. AES has been used after sample cleaning procedure to check the purity of the Cu(100) surface. The data has been processed by a computer script Analyze Auger in ImageJ and the Average Peak-to-Peak height (APPH) has been used for the quantitative analysis. The AES spectra were measured by Cylindrical Mirror Analyser with a concentric electron gun. The source of primary

4.2. DEPOSITION

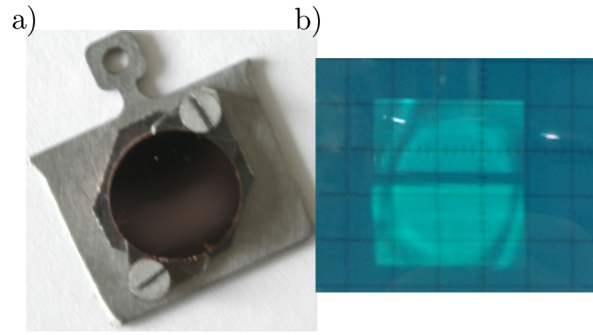


Figure 4.1: Sample Cu(100) on a sample holder. (a) outside of the chamber and (b) observed during scanning on a screen of an oscilloscope connected to an ampermeter and the x-y scanning unit of the ion gun.

electrons was a tungsten cathode, accelerated by a voltage of 3 keV and focused to a beam with ~ 0.5 mm diameter. The beam had a perpendicular incidence to the surface.

Deposition was performed by two different evaporators. One of them, the Omicron EFM3-T is a triple evaporator, allowing mounting of three various compounds for evaporation, which proved crucial when investigating the Ni concentration dependence. Evaporation rods of Fe, $\text{Fe}_{85}\text{Ni}_{15}$ and $\text{Fe}_{64}\text{Ni}_{36}$ were mounted in cells of the evaporator. The second evaporator was a single Omicron EFM3 with a $\text{Fe}_{78}\text{Ni}_{22}$ compound. Prior and after the deposition a Quartz Crystal Monitor check has been performed. The QCM temperature had to be calibrated (figure 4.2).

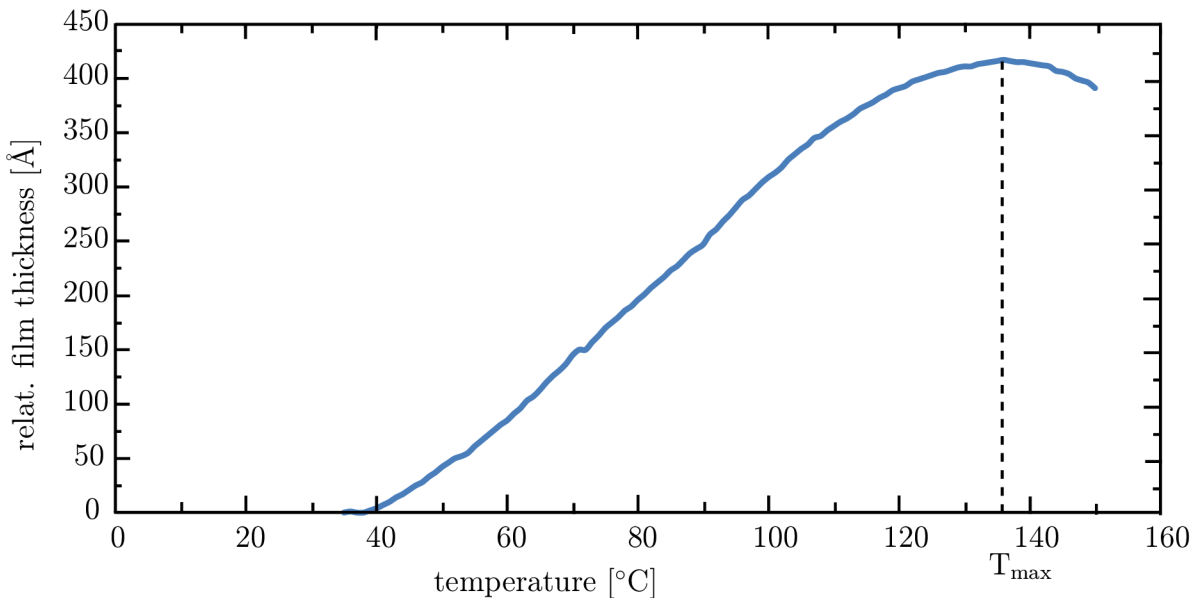


Figure 4.2: QCM calibration curve. The curve portrays the dependency of relative thickness of the film measured by the QCM, which is dependent on the temperature of the quartz crystal. The temperature $T_{\max} = 138^\circ\text{C}$ has been selected because the calibration curve has the lowest gradient around this temperature.

4. DEPOSITION OF THIN Fe_xNi_{1-x}/Cu FILMS

The expected interlayer distances of a fcc(100) Fe is ~ 0.180 nm [1] and thus the corresponding thickness of a 44 ML thick film is 7.92 nm. This was approximated to 8 nm throughout the investigation. The reason was that the evaporation rate during every deposition was decreasing. Consequently, the thickness of the film was usually lower than planned and a +0.1 nm was a suitable offset for the thickness calculation. The length of an evaporation rod has diminished throughout the evaporation; therefore it has been pushed inward in order to keep the evaporation running at a steady speed.

A large number of depositions has been performed. Following list gives the usual order of experiments with their typical parameters:

1. Crystal inserted in the chamber loadlock
2. Bakeout of the loadlock - power to 4A @ 100V (60%)
3. Cleaning of the crystal (3 cycles) sputtering 40 minutes with 2 keV Ar ions, $I_{\text{manipulator}} = 8\mu\text{A}$ then annealing 10 minutes at 520°C by electron bombardment of the back of the sample holder
4. AES purity check on three different places
5. QCM check of the deposition speed
6. Deposition - parameters will be displayed when discussing different Fe-Ni alloys. Note that the flux monitor (figure 2.1) of the evaporator was biased with the voltage of 1.5 keV. This served as a potential barrier for the ions emitted from the evaporator, which could eventually transform our metastable films.
7. LEED analysis typically with 120eV, $I_{\text{filament}} = 1.41\text{A}$
8. AES analysis focused on C, O and Fe-Ni ratio
9. SMOKE analysis
10. Transformation with 2 keV Ar ions, $I_{\text{sample}} \sim 0.45\mu\text{A}$, $p_{\text{Ar}} \sim 2.7 \times 10^{-7}$ millibar, single dose defined as $3 \times 10^{15}\text{cm}^{-2}$
11. LEED analysis
12. SMOKE analysis

4.3. Growth of metastable $Fe_{85}Ni_{15}/Cu(100)$

In section 2.6.4, we have described the conclusion of the research performed by Shah Zaman, which was that 15% of Ni are necessary in a Fe-Ni alloy to grow a 44 ML thick metastable film. This conclusion was confirmed by STM images in figure 2.12. On the base of previous investigation, we have mounted an evaporation rod with the $Fe_{85}Ni_{15}$ alloy in the EFM3T evaporator. The typical deposition parameters are summarized in table 4.1.

Table 4.1: Typical Evaporation Parameters for $Fe_{85}Ni_{15}$ Alloy in the EFM3T Evaporator

High Voltage	I_{filament}	I_{emission}	Flux	Deposition Rate	Pressure
800 V	2.1 A	12 mA	86 nA	$90 \text{ s}\text{\AA}^{-1}$	2×10^{-10} millibar

In the course of repeating the experiment, we found that the stability of the film is strongly dependent upon the pressure in the chamber. The first deposition in figure 4.3(a) was done at pressure 1×10^{-9} and the film could not have been transformed even after

4.3. GROWTH OF METASTABLE $FE_{85}NI_{15}/CU(100)$

prolonged irradiation by 2 keV Ar ions. The cause for higher pressure during deposition was that the evaporator has not been well degassed and the evaporation rod was new. When looking at both the SMOKE and LEED data, we can see that the film grew in the non-magnetic fcc phase and CO dissociation took place during deposition. The LEED pattern of as deposited film shows (1,0) and (1,1) fcc Fe spots and additional (1/2, 1/2) spots, forming a $c(2 \times 2)$ oxygen superstructure. The properties of the film did not change after irradiation, except for the removal of the $c(2 \times 2)$ -O superstructure showed in LEED. This means that the film is stable, which was unexpected because Shah Zaman reported that only films with higher Ni content [21% in figure 2.12(e,f)] grow in stable fcc phase.

After this unexpected result, the evaporator has been well degassed and the experiment was repeated [figure 4.3(b)]. Now, the pressure during deposition was roughly 4×10^{-11} millibars and the film exhibited properties which were described by Shah Zaman's STM measurements in figure 2.12(b-d). We have looked through the data recorded by Shah Zaman and the pressure during deposition of the film with 15% of Ni has been below 1×10^{-10} millibar, i.e. outside of the range of the Penning gauge. It must be noted that the Penning gauge has a very high uncertainty when measuring the pressure, namely at the low edge of its range. We have, however, recorded the pressure using a Bayard-Alpert gauge, which has higher sensitivity and its range is roughly 2 orders of magnitude lower than the Penning gauge. It might be therefore concluded that the pressure during deposition in the STM chamber equals roughly to the pressure 4×10^{-10} millibar in the SMOKE system. The SMOKE data suggest that a magnetic transformation took place upon single-dose 2 keV Ar ion beam irradiation, which is equal to 3×10^{15} cm⁻². This conclusion is also supported by LEED, which further shows that the CO dissociation took place during the deposition.

The next reported deposition in figure 4.3(c) has been performed with the cryo-baffle filled with liquid nitrogen and after three TSP cycles. The pressure during deposition was therefore below 5×10^{-11} millibar. At this point we observe that the films grew with some areas already transformed. The single-dose-irradiation shows, however, that it has not been fully transformed after deposition. The LEED patterns show the fcc structure after deposition with some interesting domains surrounding each of the fcc points. It is worth noting that no $c(2 \times 2)$ -O superstructure is visible in LEED. From this fact it might be argued that without the surfactant effect of oxygen, the growth mode of the film is not the layer-by-layer growth. It has been mentioned in section 2.6.3 that the effect of oxygen serves as a surfactant. The lack of oxygen could therefore allow the growth of various domains and islands, which then resulted in LEED observed in figure 4.3(c).

4. DEPOSITION OF THIN Fe_xNi_{1-x}/Cu FILMS

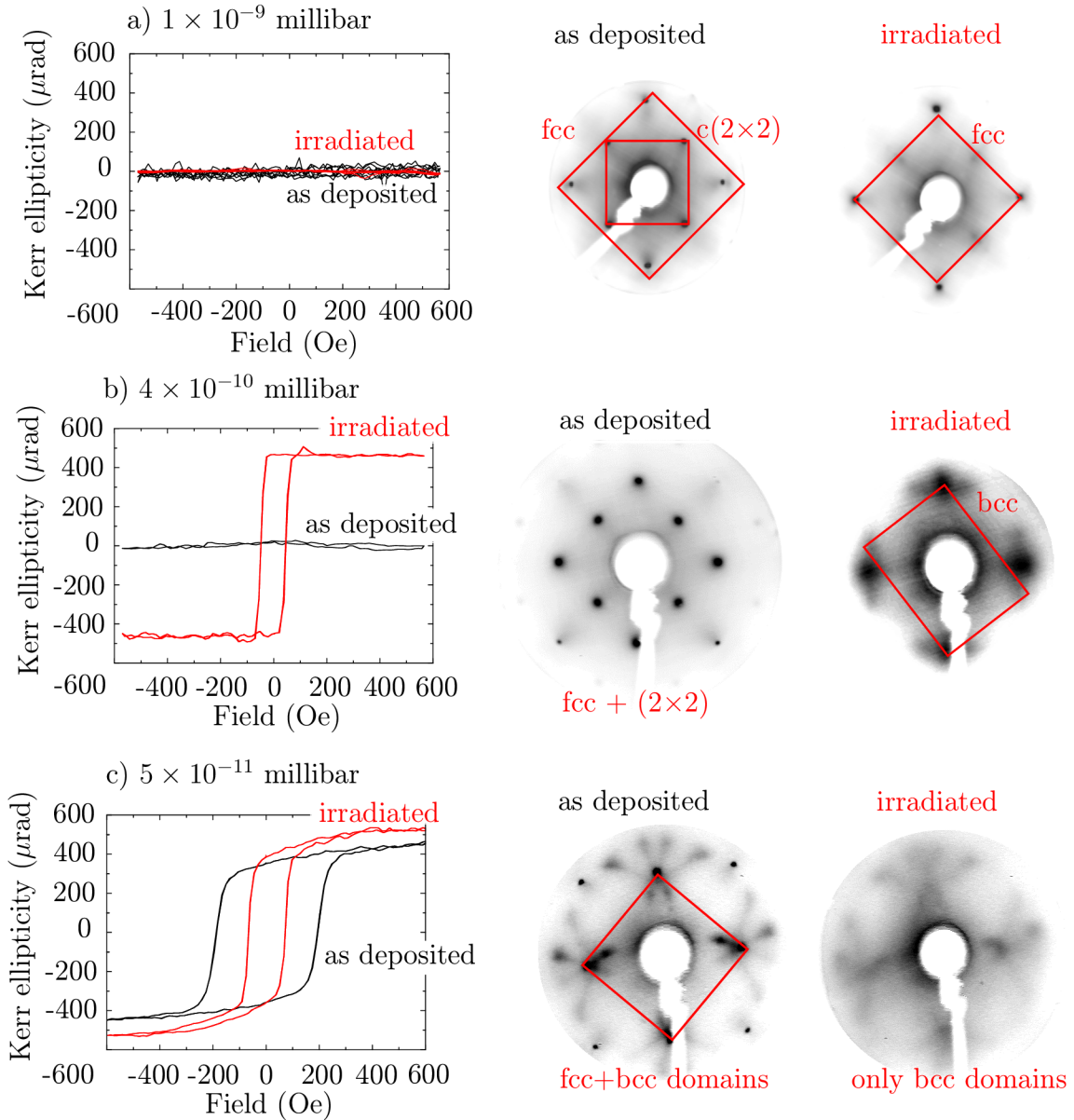


Figure 4.3: SMOKE and LEED measurements of as-grown and transformed 44 ML $Fe_{85}Ni_{15}$ films grown at different pressures. (a) Growth of non-transformable fcc γ Fe at 1×10^{-9} millibar during deposition: SMOKE shows no magnetic transformation after irradiation with an 2 keV Ar ion dose of $3 \times 10^{16} \text{ cm}^{-2}$. The LEED pattern of as deposited film shows the c(2 \times 2)-O superstructure on top of the fcc. The irradiated film shows removal of the O superstructure. (b) Deposition of metastable fcc c-Fe at a pressure of 4×10^{-11} millibars: Irradiation with an ion dose of $3 \times 10^{15} \text{ cm}^{-2}$ transforms the film to ferromagnetic. The LEED pattern of as deposited film is similar to (a). The irradiated film shows the bcc structure and partial removal of the O superstructure. (c) The film grown at the pressure of 5×10^{-11} millibars is spontaneously transformed into bcc. The transformation was completed by irradiation with $3 \times 10^{15} \text{ cm}^{-2}$ Ar ions. According to LEED, the as deposited film shows a fcc structure with a few domains. The fcc structure is destroyed upon ion beam irradiation and the domains remain on the surface.

4.4. Growth of metastable $Fe_xNi_{1-x}/Cu(100)$

Next series of experiments was performed in order to find a Ni-concentration which would allow us to grow metastable fcc Fe-Ni films. We found that the correct composition is one with $\sim 23\%$ of Ni. Figure 4.4 shows SMOKE and LEED measurements after deposition and after irradiation. The film measured after deposition exhibits no magnetization (the black SMOKE curve) and has a fcc reconstruction, as measured by LEED. It is worth noting that the LEED was measured approximately 12 hours after the deposition and therefore some CO dissociation already took place. The adsorbed oxygen then formed the $c(2 \times 2)$ superstructure (section 2.6.3) visible in LEED pattern. The film has then been transformed by two consequent doses, $3 \times 10^{15} \text{ cm}^{-2}$ each. This dose was chosen on the base of the experiments of Shah Zaman, where she completely transformed a 44 ML thick $Fe_{85}Ni_{15}$ film. We can see that the first dose (the green SMOKE curve) transformed the film only partially, in contrast to the findings of Shah Zaman. The SMOKE measurement after the second irradiation (total dose was $6 \times 10^{15} \text{ cm}^{-2}$) shows a completely transformed film.

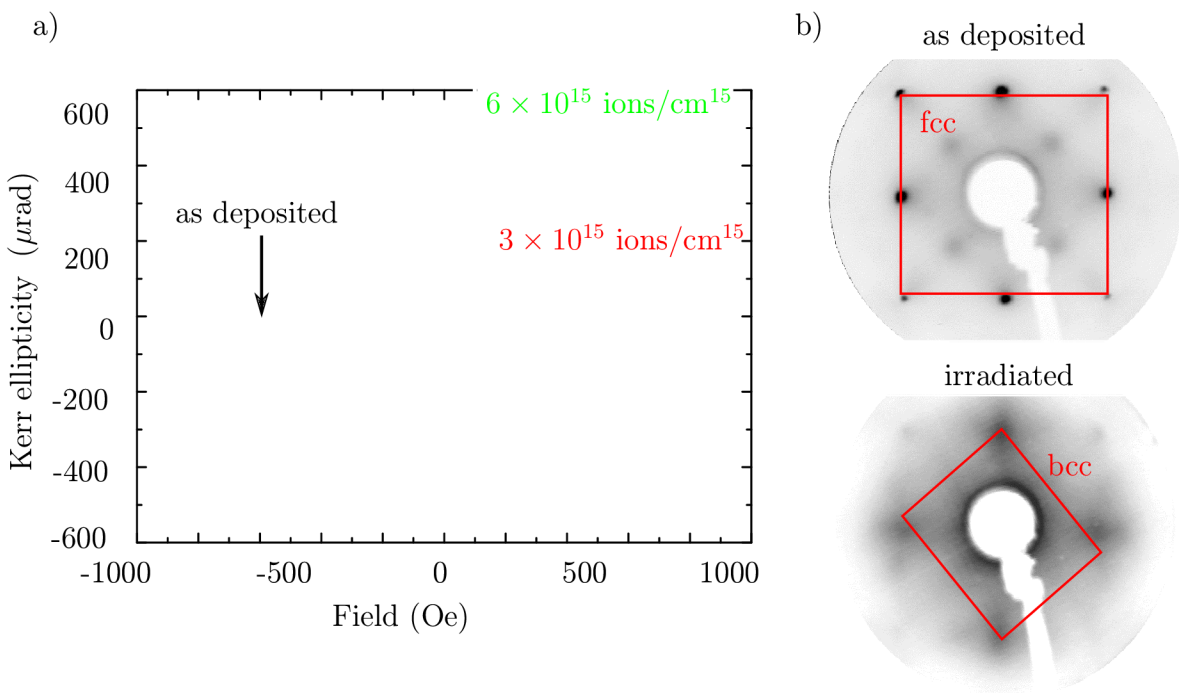


Figure 4.4: (a) SMOKE measurements of a metastable $Fe_{77}Ni_{23}$ layer deposited at a base pressure 3×10^{-9} mbar millibars. The as deposited film is nonmagnetic (black). The film partially transforms to bcc after irradiation with an ion dose of $3 \times 10^{15} \text{ cm}^{-2}$ (red). Full transformation is achieved after an ion dose of $6 \times 10^{15} \text{ cm}^{-2}$ (green). (b) The LEED pattern of the as-deposited film shows an fcc lattice with a very weak $c(2 \times 2)$ -O superstructure. After irradiation ($6 \times 10^{15} \text{ cm}^{-2}$), the bcc structure is observed.

4.5. Phase diagram of Fe and Ni

In course of performing the experiments with co-evaporation of Fe and Ni, we found that the concentration of Ni is not the only factor responsible for the film stability and that the role of interstitial C caused by dissociation of CO [26, 4] must be taken into account. To find out the interplay between Ni and CO, we extended the series of experiments from figures 4.4, 4.3 and 2.12 by depositing 44 ML thick films with different Ni concentrations at different residual background pressures.

In figure 4.5, we have summarized our experiments in a phase diagram of the dependency of structural and magnetic phase of Fe_xNi_{1-x} films on Ni concentration and on residual gas pressure during deposition. The phase diagram reveals three distinct regions:

1. ferromagnetic bcc when the Ni concentration and the residual gas pressure during deposition are low (bcc-FM region);
2. stable, i.e., non-transformable, nonmagnetic fcc at high Ni concentration and high residual gas pressure (fcc-NM region), and a
3. metastable region in between. These metastable fcc Fe films are suitable for ion-induced transformation. The films in the metastable region of the phase diagram grow in the fcc γ phase.

These three regions have been clearly distinguished in both the STM and SMOKE setups.

First, let us look at the STM investigation. As can be seen from the STM image of the film with 15% Ni concentration [figure 2.12(b)], the film grows layer by layer and only a few isolated bcc needles can be found. Ion irradiation creates bcc needles in the film initially oriented along the close-packed $[011]$ and $[01\bar{1}]$ directions [3], and later growing in size into a randomly oriented larger patches [figure 2.12(c,d)]. The cause of this randomness is that the bcc needles formed with the initial ion doses move stabilizing agents in the film, which then start clustering. High density of interstitials then hinders further growth of bcc needles and pushes them in random directions.

The experiments done in the SMOKE UHV setup help us understand the role of the residual background pressure. The films with a Ni concentration of 15% showed completely different behaviour dependent on the residual gas pressure during deposition: Deposition at a pressure of 1×10^{-9} millibar leads to non-transformable fcc films; deposition at 9×10^{-11} millibar or below leads to a spontaneous fcc-bcc transformation; the metastable range needed for the ion-induced fcc-bcc transformation is in between. Thus, at low residual gas pressures, 15% concentration of Ni alone is not sufficient to stabilize the fcc γ phase. As residual gas analysis showed a dominant CO peak during deposition, we conclude that interstitial C together with Ni is responsible for the stability of the fcc γ phase at these values of the Ni concentration, similar to the effect of CO on clean Fe films. This notion is also supported by the LEED patterns of films deposited at higher residual background pressures showing a clear $c(2 \times 2)$ superstructure, which can be explained by oxygen floating at the surface; the carbon created upon dissociation of CO is incorporated in the growing film. The additional stabilizing effect of carbon can even hinder the ion-induced transformation as can be seen in case of films grown at the pressures above 1×10^{-9} millibar. In order to find the Ni concentration sufficient to stabilize the fcc γ phase without the help of interstitial C, the pressure in the SMOKE chamber was reduced to below 3×10^{-11} . We found that at this low pressure, the minimum Ni concentration

4.5. PHASE DIAGRAM OF FE AND NI

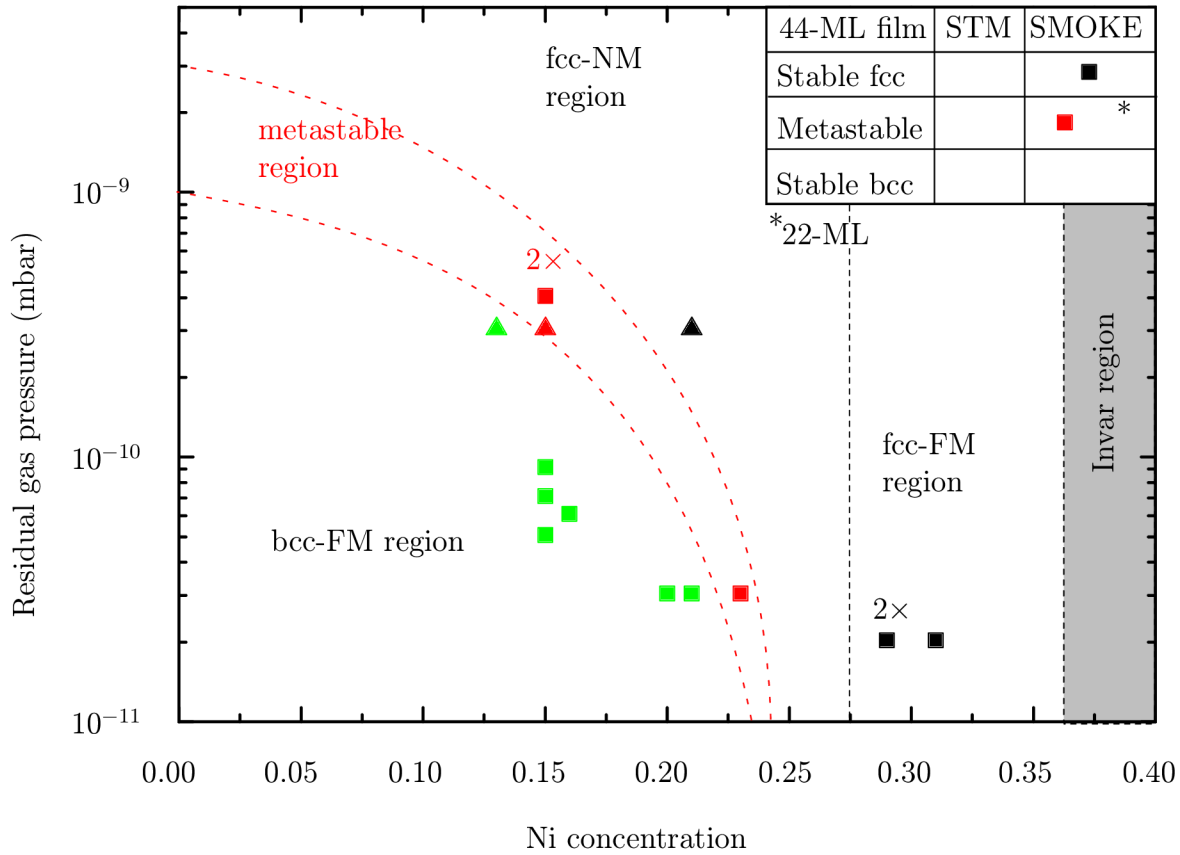


Figure 4.5: Experimentally determined phase diagram of the dependency of the structural and magnetic phases of $\text{Fe}_x\text{Ni}_{1-x}$ films on Ni concentration and on the residual gas pressure during a deposition. The data are combined from the experiments done in the SMOKE and STM UHV setups. The CO stabilized 22 ML thick film [4] is marked by an asterisk. Red dotted lines show the approximately linear Ni-concentration dependence of the boundaries of the metastable region. At Ni concentrations above 28%, the films are fcc ferromagnetic (black dotted line).

needed to stabilize the fcc γ phase during growth is 23%. This film is transformable by ion bombardment, but full transformation requires a higher ion dose than in case of the films stabilized with combination of C and Ni 4.4. The LEED measurements prove that only a small amount of CO was adsorbed as the $(1/2, 1/2)$ spots caused by the $c(2 \times 2)$ -O superstructure are weak.

5. The effect of CO and O₂ on growth of 44 ML Fe₇₈Ni₂₂ films

In order to be able to grow the metastable films at laboratories of the Institute of Mechanical Engineering (IPE) at the Faculty of Mechanical Engineering (FME) of the Brno University of Technology (BUT), we need to rule out the delicate dependency of the stability of the film on the pressure inside of the chamber 4.5. For this, we chose to grow the 44 ML thick Fe₇₈Ni₂₂/Cu(100), which grows in the metastable form in case that it is not affected by any other stabilizing agent. For UHV chambers which have the lowest pressure during deposition in the order of 1×10^{-9} millibar is the gas with highest concentration (when not considering H) CO emitted from the evaporator. It has already been mentioned in section 2.6.3 that the CO dissociates on the surface of Fe and supports the stability of the film.

In this chapter, we will first investigate the effect of increased CO pressure on the 44 ML thick Fe₇₈Ni₂₂ film during deposition, and how the effect of CO can be effectively removed. In order to rule out this stabilizing effect and to leave the Ni as the sole stabilizing agent, we have decided to saturate the surface of our film with O, which prohibits the CO dissociation, as shown in [4]. Some extra experiments will also be presented in order to obtain a deeper insight into the system.

5.1. Saturation of O in order to prevent the stabilizing CO effect

Let us refer back to the phase diagram (figure 4.5). We can see that the Fe₇₈Ni₂₂ film should grow as stable, non-magnetic fcc in the event that the pressure in the chamber is higher than 1×10^{-9} millibar. We decided to perform two experiments with this pressure of CO in the chamber. In the first situation, the whole deposition is performed without any change and in the second situation, oxygen is deposited on top of the first grown 11 ML in order to prohibit further CO dissociation. The usual parameters of the deposition are demonstrated in table 5.1:

Table 5.1: Typical Evaporation Parameters for Fe₇₈Ni₂₂ Alloy in the EFM3 Evaporator

High Voltage	I _{filament}	I _{emission}	Flux	Deposition Rate	Pressure
830 V	2.1 A	13 mA	27 nA	80 Å ⁻¹	1×10^{-10} millibar CO

5.1.1. The film grown in 1×10^{-9} millibar CO

As could be seen from the phase diagram, the film with 15% of Ni grew in stable form in 1×10^{-9} millibar CO. We have therefore commenced a very similar experiment with the Fe₇₈Ni₂₂ alloy, to see whether the proposed model holds also for higher Ni content and whether or not can it be used for depositions in bad vacuum. Figure 5.1 shows the SMOKE and LEED analysis of the system. As was expected, it is fcc non-magnetic after deposition (the black line) and has the c(2×2) O superstructure. Irradiation of the film

5.1. SATURATION OF O IN ORDER TO PREVENT THE STABILIZING CO EFFECT

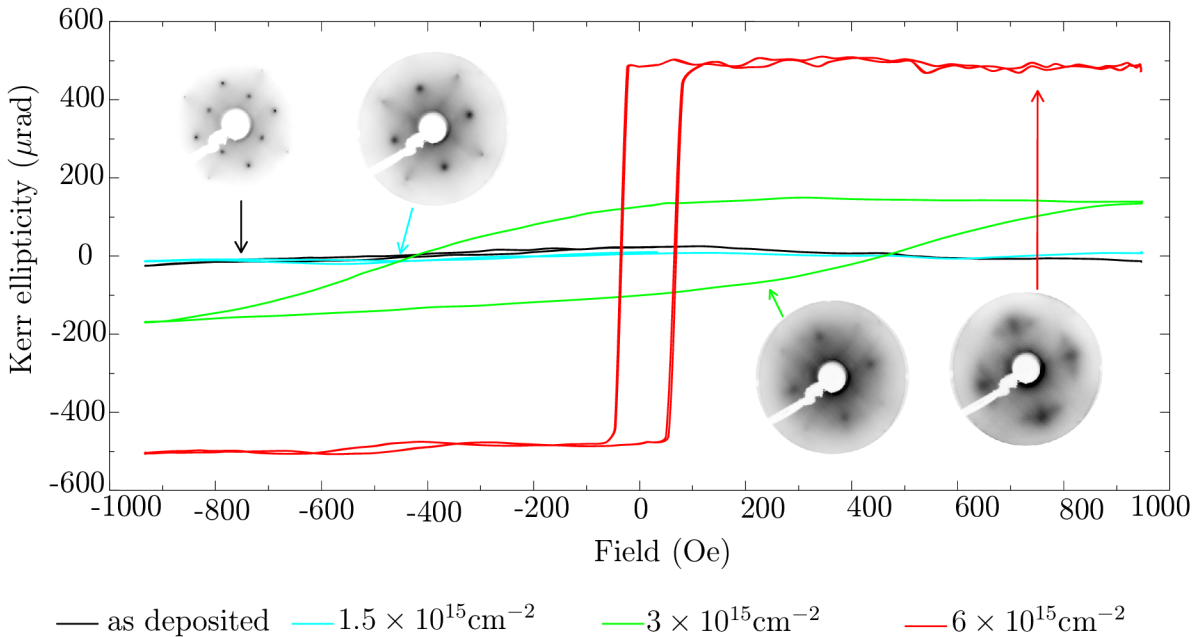


Figure 5.1: Transformation of 44 ML $\text{Fe}_{78}\text{Ni}_{22}$ grown in 1×10^{-9} millibar CO.

with half-dose ($1.5 \times 10^{15} \text{cm}^{-2}$ - the magenta line) did not change the magnetic properties of the film, but it removed the O; also the (1,0) LEED spots are more pronounced. Single dose ion irradiation (the green line) already transformed some of the film and the saturation is roughly $200 \mu\text{rad}$. The LEED pattern of the film shows nearly complete removal of the (1,1) LEED spots and even more pronounced (1,0) spots. Finally, double dose (the red line) completely transforms the film and the saturation is now roughly $500 \mu\text{rad}$, which is comparable to the saturation of the $\text{Fe}_{77}\text{Ni}_{33}$ film in figure 4.4. This is a rather unexpected result, which shows that the CO does not have a significant stabilizing effect on the $\text{Fe}_{78}\text{Ni}_{22}$ alloy. The result will be further discussed in a summary at the end of this chapter.

5.1.2. The film grown in 1×10^{-9} millibar CO, artificial O saturation after 11 ML

In this experiment, we deposited a thin layer (11 ML) of $\text{Fe}_{78}\text{Ni}_{22}$ in 1×10^{-9} millibar CO on top of the clean Cu(100) single-crystal. We choose this thickness because according to the diagram in figure 2.7, the Fe film undergoes phase and structural changes when growing epitaxially on Cu(100) below 10 ML thickness. On the other hand, we wanted to have a lowest possible thickness of the film stabilized by C. We could not deposit O_2 directly on Cu, because it does not dissociate on Cu at RT. It dissociates, however, on Fe. The deposition of the film and its characteristics after deposition are described in the last part of the schematic in figure 5.2. We can expect that the first part of the film (before O saturation) is stabilized by both the C and Ni. The rest of the film should grow as metastable, since no CO dissociation should take place. This hypothesis has been confirmed by the transformation of the film.

Figure 5.3 shows a combined LEED-SMOKE data. Here we can see that after the deposition, the film is non-magnetic and has a fcc structure. The film was then irradiated

5. THE EFFECT OF CO AND O₂ ON GROWTH OF 44 ML Fe₇₈Ni₂₂ FILMS

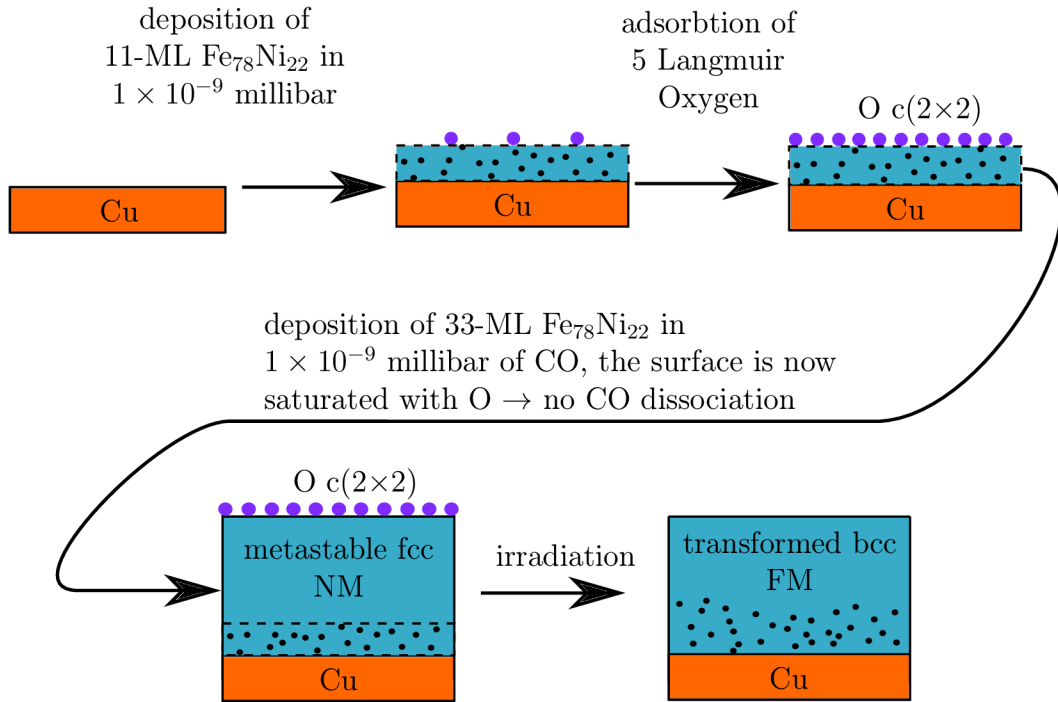


Figure 5.2: Schematic diagram of the experiment. The film was grown in 1×10^{-9} millibar CO. In the moment that approximately quarter of the film was completed, 5 Langmuir oxygen have been deposited onto the surface. The total film thickness was 44 ML and the first 11 MLs of it should have been stabilized by both C and Ni and the other half only with Ni. The C from the first quarter spreads over the volume upon ion-beam irradiation.

with two consequent Ar doses, $3 \times 10^{15} \text{cm}^{-2}$ each. The SMOKE data indicate that the film was not transformed after deposition (black line) and fully (green and red lines) transformed after the first and the second dose. The LEED data show the reconstruction of the film before and after transformation and confirm the SMOKE data. Dissociation of O₂ and creation of the c(2 × 2) superstructure has also been confirmed.

5.1. SATURATION OF O IN ORDER TO PREVENT THE STABILIZING CO EFFECT

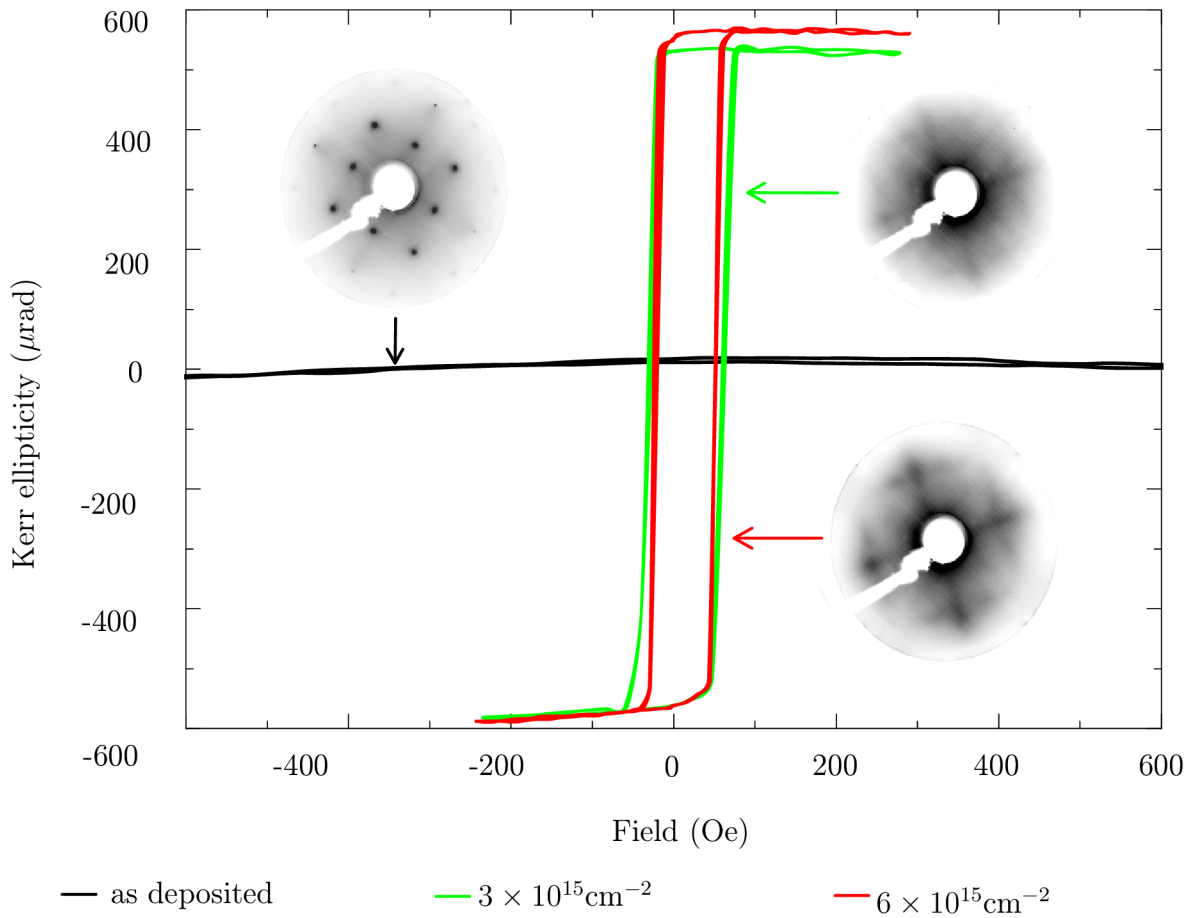


Figure 5.3: Transformation of 44 ML $\text{Fe}_{78}\text{Ni}_{22}$ grown in 1×10^{-9} millibar CO. The film was saturated after the growth of 11 ML, similar to the scheme in figure 5.2. We can observe that the film is transformed after the first Ar ion dose and the transformation is completed after double dose. LEED patterns confirm the SMOKE measurements by showing a gradual fcc-to-bcc transformation.

5.1.3. The film grown in 1×10^{-9} millibar CO, artificial oxygen saturation after 22 ML

This experiment was very similar to the previous one, with the exception that we have deposited the O₂ after depositing half of the of Fe₇₈Ni₂₂ film. Figure 5.4 gives an account of the deposition. We have deposited 5 Langmuirs of O₂ (7.5×10^{-9} millibar for 500 s) on top of the 4 nm Fe₇₈Ni₂₂ during the deposition. The change of the surface reconstruction has been confirmed real-time in LEED during a separate deposition and is included as an attachment to this thesis. The deposition then proceeded and a 8 nm thick film was completed.

The expected result of this experiment was that the first 22 ML of the film would be stabilized by both Ni and C and the next 22 ML will be stabilized only by Ni. Figure 5.5 shows a combined LEED-SMOKE data. Here we can see that after the deposition, the film is non-magnetic and has a fcc structure. The film was then irradiated with two consequent Ar doses, each of which was $3 \times 10^{15} \text{cm}^{-2}$. The SMOKE data indicate that the film was partially (green line) and fully (red line) transformed after the first and the second dose. The LEED data show the reconstruction of the film before and after irradiation. The LEED after irradiation shows that the surface is transformed from fcc to bcc. These data are very well in line with the previous experiment, when we deposited the same film at the same CO pressure, without the artificial O saturation.

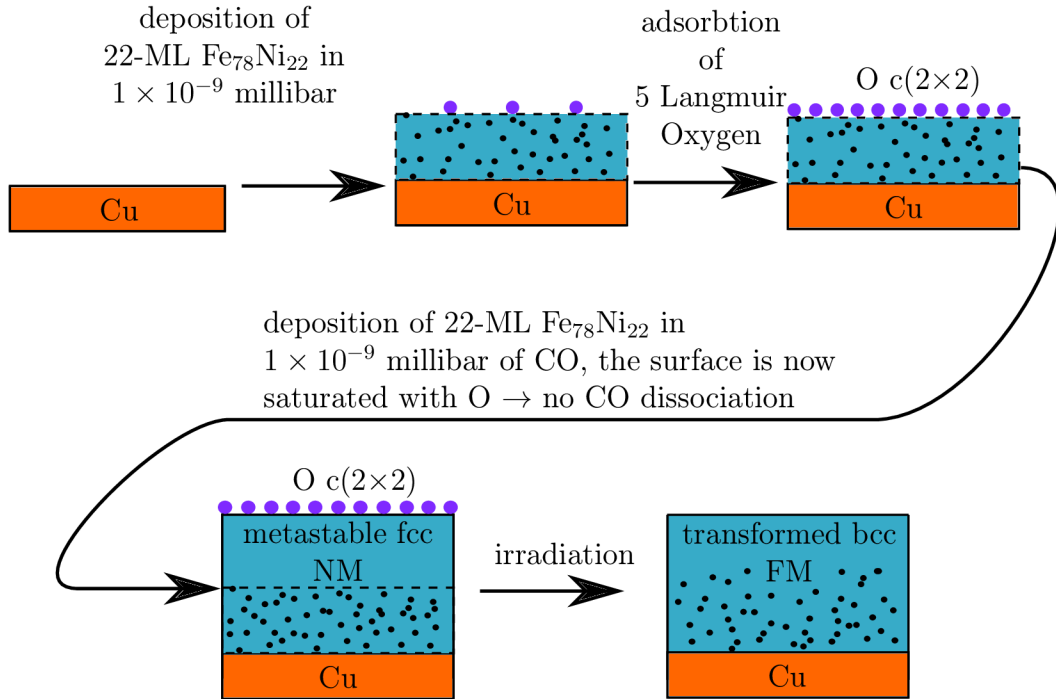


Figure 5.4: Schematic diagram of the experiment. The film was grown in 1×10^{-9} millibar CO. The moment when approximately half of the film was completed, 5 Langmuir oxygen has been deposited on the surface. The total film thickness was 44 ML and half of it should have been stabilized by both C and Ni, and the other half by Ni only.

5.2. SUMMARY OF THE EFFECT OF CO AND O ON THE $Fe_{78}Ni_{22}$

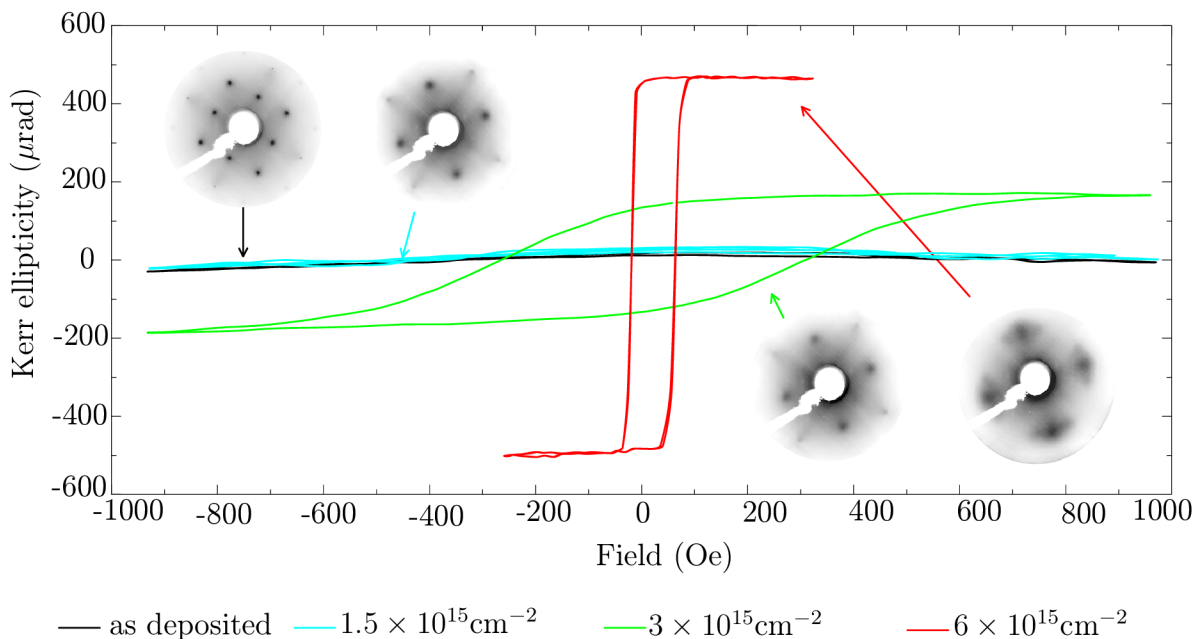


Figure 5.5: Transformation of 44 ML $Fe_{78}Ni_{22}$ grown in 1×10^{-9} millibar CO. The film was artificially saturated after the growth of 22 ML, according to the scheme in figure 5.4. We can observe that the film was gradually transformed with the increasing ion dose. LEED patterns confirm the SMOKE measurements by exhibiting a gradual fcc-to-bcc transformation.

5.1.4. The film grown in 3×10^{-9} millibar CO

As already mentioned, it has been reported by Shah Zaman that it is possible to stabilize a pure Fe film up to 22 ML at a CO pressure 3×10^{-9} millibar [16]. We have therefore decided to run an experiment to see how will this CO pressure affect the 44 ML $Fe_{78}Ni_{22}$ film. The expected result of this experiment [figure 5.6] was that the film will eventually become saturated due to the high CO concentration, and part of it should be transformable. The film was deposited and consequently irradiated. Corresponding data are shown in figure 5.7.

Saturation of 200 μ rad was measured (SMOKE hysteresis curve in figure 5.7), which is very similar to the one measured on a $Fe_{78}Ni_{22}$ film grown at low pressure (figure 4.4). The LEED data confirm the conclusion that the film is fcc after deposition and partly transformed after irradiation, with some areas still fcc. This experiment therefore produced an interesting result which does not correspond to the phase diagram. In the phase diagram, we can observe that the effect of 3×10^{-9} millibar CO on a 44 ML thick film with 22% should be stabilizing - the film should grow as stable fcc.

5.2. Summary of the effect of CO and O on the $Fe_{78}Ni_{22}$

When performing experiments with artificial CO dosing during deposition of 44 ML $Fe_{78}Ni_{22}$ on Cu(100), we came to the following conclusions:

- the CO has some stabilizing effect on the film with 22% Ni,

5. THE EFFECT OF CO AND O₂ ON GROWTH OF 44 ML Fe₇₈Ni₂₂ FILMS

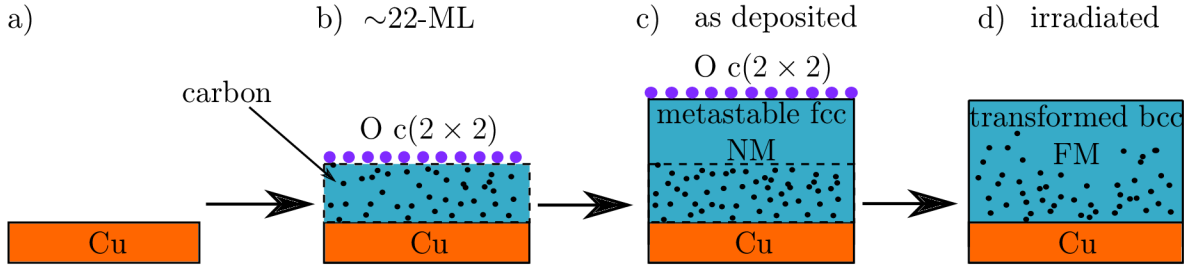


Figure 5.6: Scheme of the experiment of 44 ML Fe₇₈Ni₂₂ grown in 3×10^{-9} millibar CO. On a clean crystal Cu(100) (a) is deposited Fe₇₈Ni₂₂ in 3×10^{-9} millibar of CO. The surface should get saturated with O₂ after the growth of roughly 22 ML and form the c(2 × 2) superstructure; carbon remains in the film in the form of interstitial atoms (b). The film then grows on and no CO dissociation takes place → no interstitial carbon (c). The irradiation dose in (d) was $3 \times 10^{15} \text{cm}^{-2}$.

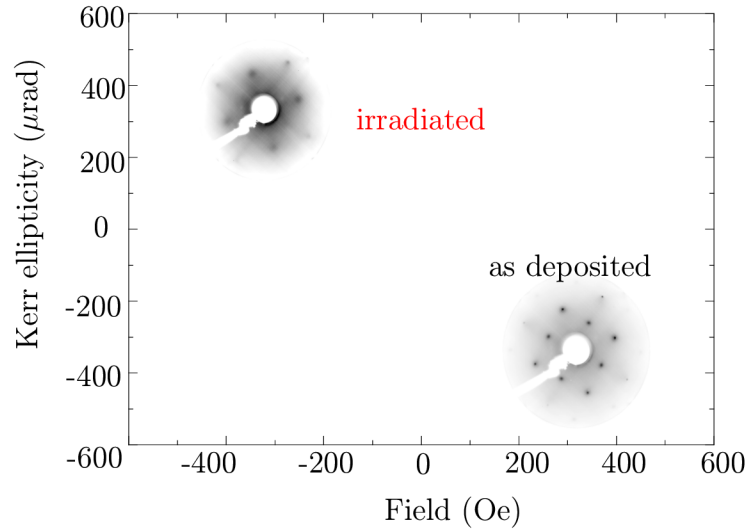


Figure 5.7: SMOKE and LEED analysis before and after transformation. The irradiation dose was $3 \times 10^{15} \text{cm}^{-2}$.

- this stabilizing effect can be removed by artificial saturation of the surface with O,
- the pressure of CO that fully stabilized the fcc phase of a film with 15% Ni does not stabilize a film with 22% Ni, i.e. the film with 22% Ni could always be transformed.

The purpose of the investigation of the effect of CO on our films was to give some experimental foundation to growth of thin films of Fe₇₈Ni₂₂/Cu(100) in chambers with higher base pressure. It has been demonstrated that the CO has some stabilizing effect on the film 5.1, although surprisingly, the pressures we have investigated never led to a total stabilization of the film as was in the case of Fe₈₅Ni₁₅.

The most probable reasons for this difference in behaviour should be associated with the amount of the CO dissociated. With less CO dissociation, there was less C that supported the stable fcc form in the bulk. One of the reasons for lower CO dissociation can include the fact that the pressure in the chamber during the growth of Fe₈₅Ni₁₅ did not correspond to the pressure on the sample. The reason for this claim is that the

5.2. SUMMARY OF THE EFFECT OF CO AND O ON THE $Fe_{78}Ni_{22}$

back-pressure reported in the phase diagram (4.5) was created by the evaporator, since it was not well degassed. The CO molecules leaving the evaporator should have had higher partial pressure in the direction it was aiming at - which means on the sample as well. The pressure on the sample in case of the deposition of $Fe_{78}Ni_{22}$ was, on the other hand, very well defined by precise dosing through of the leak valve. A joint effect to the one mentioned above is that the Fe catalyses CO dissociation and the lower amount of Fe in $Fe_{78}Ni_{22}$ led to a lower rate of CO dissociation, which in turn gave less C to support the stable phase of the film.

AES measurements were performed after each deposition and irradiation. We have observed the following:

- the amount of Ar was increasing after irradiation, which is obviously attributed to absorbed ions,
- C signal was increasing as well. The reason for this is that C was deposited (from the gasses in the chamber) during ion beam irradiation,
- In case that the deposition was performed in CO, the O signal was also observed. The O signal was decreasing with irradiation. It has stopped, however, at approximately 1/3 of its saturation value, which could be attributed to some O atoms absorbed in the bulk,
- the amount of Ni was kept constant over the surface of the crystal even after prolonged irradiation.

6. Magnetic Nanostructures in 44 ML $Fe_{78}Ni_{22}$ films

Even though no metastable alloys of Fe and Ni have been grown at the laboratories of IPE FME BUT, we proceeded with research in magnetic nanopatterning on the films deposited at the TU Wien. In previous chapters, we have demonstrated that we have succeeded in growing metastable films of Fe alloyed with Ni on Cu(100). These films are good candidates for ion-beam-induced structural and corresponding magnetic transformation. This chapter focuses on preparation of magnetic nanostructures in thin films of $Fe_{78}Ni_{22}$ by FIB and their analysis via AFM and MFM.

After deposition at the TU Wien, 8 ML thick $Fe_{85}Ni_{15}$ films have been brought to the laboratories at the IPE FME BUT. Here, at the BUT, these films have been nanopatterned (e.g. see figure 6.2) in the combined SEM/FIB system, discussed in section 3.1.2. The FIB uses Ga ions, which have a different behaviour upon impact in comparison to Ar ions. Reason for this is mainly their mass and higher acceleration energies. Figure 6.1 describes the behaviour of Ga ions with energies 10, 20 and 30 keV in the film.

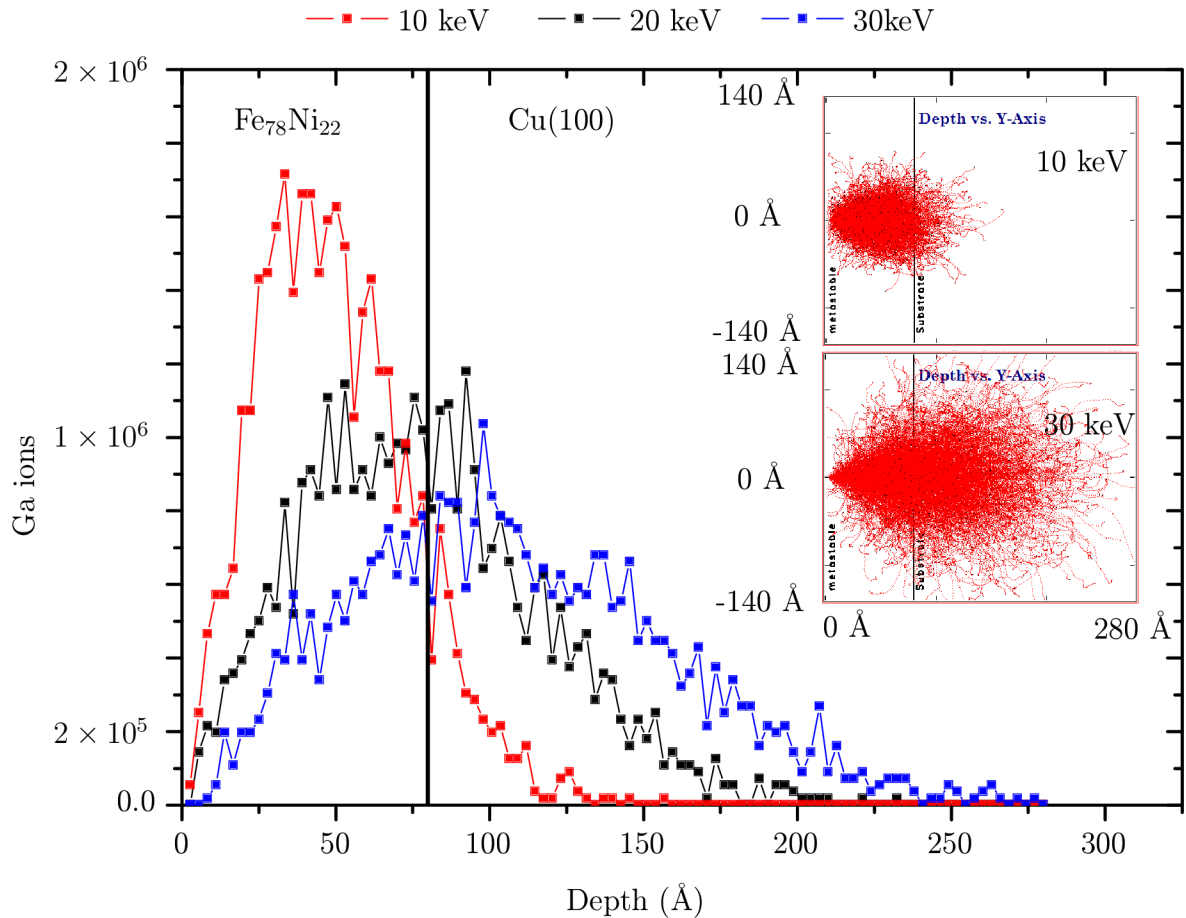


Figure 6.1: SRIM analysis of Ga ion penetration into 44 ML $Fe_{78}Ni_{22}/Cu(100)$. The insets show collision cascades for Ga ions with 10 keV and 30 keV.

6.1. MAGNETIC NANOSTRUCTURES CREATED BY 30 KEV GALLIUM IONS

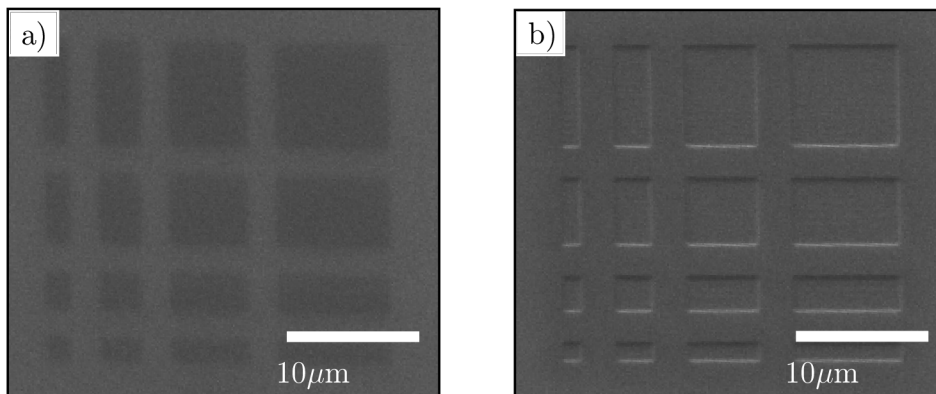


Figure 6.2: SEM analysis of micro- and nanostructures made by FIB, the energy of the electron beam was 30 keV. The SEM was taken at 55° electron incidence angle. Irradiation doses were (a) $2.5 \times 10^{15} \text{ cm}^{-2}$ and (b) $1 \times 10^{17} \text{ cm}^{-2}$. (a) exhibits only a lower emission of electrons. (b) shows that some of the film is already sputtered off.

6.1. Magnetic nanostructures created by 30 keV Gallium ions

Firstly of all we tried to create magnetic nanostructures with a 30 keV Ga ion beam. The reason was that the beam profile is of Gaussian shape and has the lowest possible spot size, which is below 10 nm. The drawback of this process is that the Ga ions penetrate deep into the sample (relative to the thickness of the film), cause intermixing on the FeNi/Cu boundary and do not have such a large cross-section as 10 keV ions.

6.1.1. Different size of patterns with different dose

In the beginning of the experiments, we tried to investigate whether we can create magnetic domains and what was the ideal size of the nano-patterns. Another aim of the following experiments was to confirm the ion dose necessary for transformation of the film, which would be different for Ga ions in comparison to Ar ions.

SEM proved to be an extremely useful tool for in-situ control of the FIB irradiation process. SEM analysis of two patterns created by 30 keV Ga ions with doses $2.5 \times 10^{15} \text{ cm}^{-2}$ [figure 6.2(a)] and $1 \times 10^{17} \text{ cm}^{-2}$ [figure 6.2(b)] confirmed that the areas (darker fields) were irradiated. The irradiated areas in figure 6.2(a) exhibit only lower emission of secondary electrons in comparison to non-irradiated surface. The irradiated areas in figure 6.2(b) lead to the conclusion that some of the film has already been sputtered off due to different contrast on the edges of these structures.

An array of such structures with different ion doses has been created. Let us now look on AFM/MFM analysis of the most interesting areas (figure 6.3) of the patterns from figure 6.2. Figure 6.3(a) is an AFM scan over the area portrayed in SEM analysis in figure 6.2(a). We can see that some surface corrugation is visible. It has the order of magnitude of Cu crystal steps, which are visible as parallel lines crossing through the image. The MFM image of the same area in (b) is much more intriguing. In the areas irradiated by FIB we can see that some bcc nucleation centres are created by the irradiation. The bcc areas show in the MFM as dipoles, which are black on one side (the magnetic tip

6. MAGNETIC NANOSTRUCTURES IN 44 ML $FE_{78}NI_{22}$ FILMS

was attracted by the magnetic field) and white on the other (the tip was repelled). The AFM scan in 6.3(c) confirms that the corrugation of the film caused by impact of Ga ions is higher with increasing Ga ion dose; the ion dose in this case was $1 \times 10^{16} \text{ cm}^{-2}$. Areas in the corresponding MFM image in (d) are now completely transformed, but we cannot observe any well-defined magnetic characteristics. Finally, some the film analysed in figure 6.3(e) is already sputtered off. The dose used for creation of these micro- and nano-structures was $2.5 \times 10^{16} \text{ cm}^{-2}$. The MFM image in (f) still shows some magnetic contrast, but we could only speculate about its properties.

These experiments confirmed that the patterns created by FIB in the films are very sensitive to the ion dose and that the ion dose slightly differs from the Ar dose used for whole-film transformation.

6.1. MAGNETIC NANOSTRUCTURES CREATED BY 30 KEV GALLIUM IONS

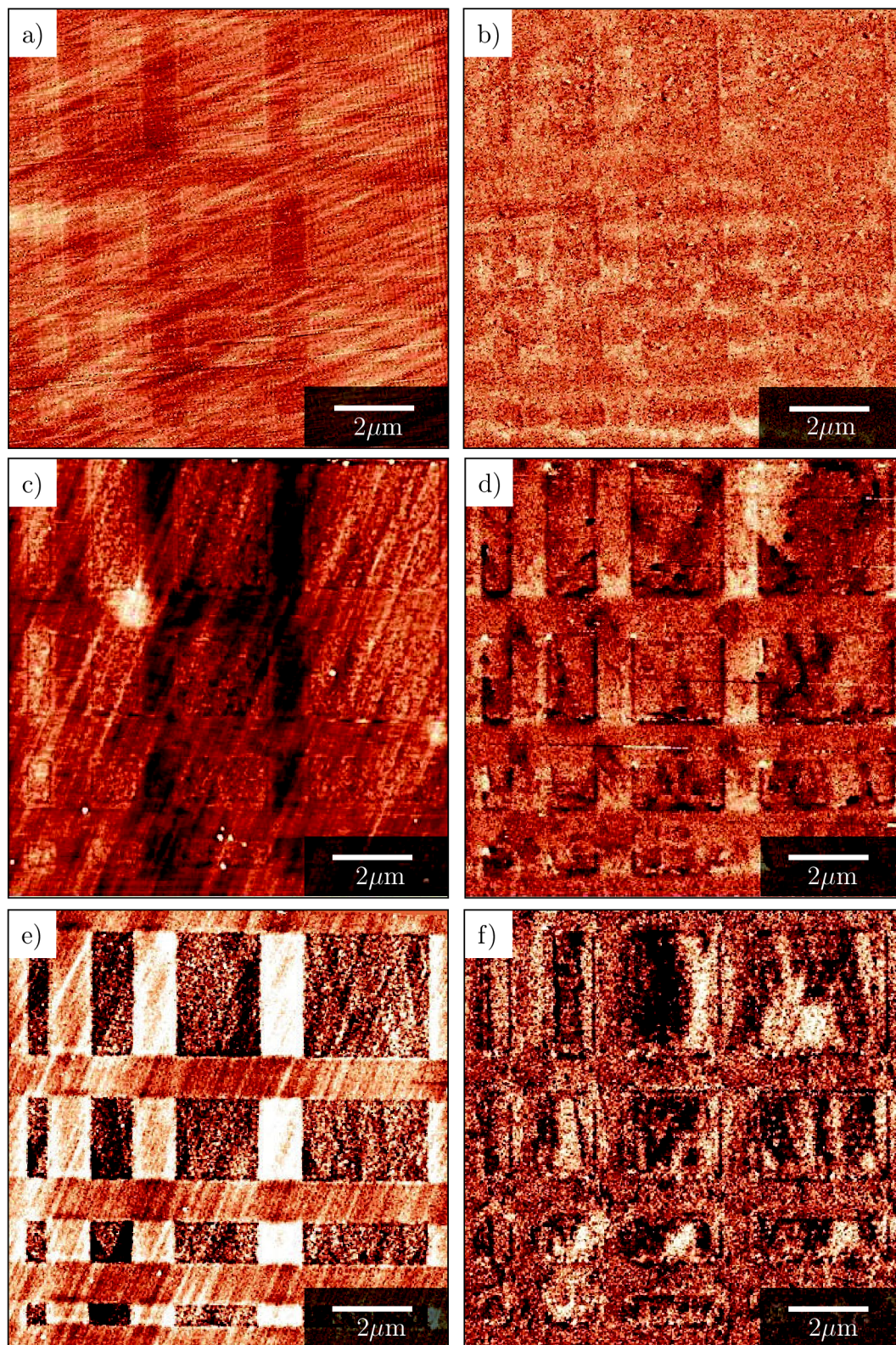


Figure 6.3: AFM (left) and MFM (right) analysis of micro- and nanostructures created by doses (a) 2.5, (b) 10, (c) $25 \times 10^{16} \text{ cm}^{-2}$. The surface corrugation is barely visible in the case of (a, c). The material has been sputtered off in (e,f). Cu step edges are clearly visible. The MFM show different behaviour for each irradiation dose.

6.1.2. Different ion dose and irradiation parameters

After the investigation of an ion dose necessary for the transformation of the film and observation of some interesting magnetic properties, we have decided to focus on the effect of different irradiation parameters. Because we have not observed any specific and well-defined behaviour corresponding to the size of the irradiated areas, we have decided to perform this investigation on the largest ($3 \times 3 \mu\text{m}^2$) squares.

Magnetic squares in figure 6.4 were created by a single scan. The film is gradually more transformed [SEM analysis in (a) has been confirmed by MFM] with increasing dose up to the point, where it is sputtered off, as confirmed by AFM. MFM detail (b) is of an area with some interesting pattern in the bottom part of the square, which is also visible in SEM.

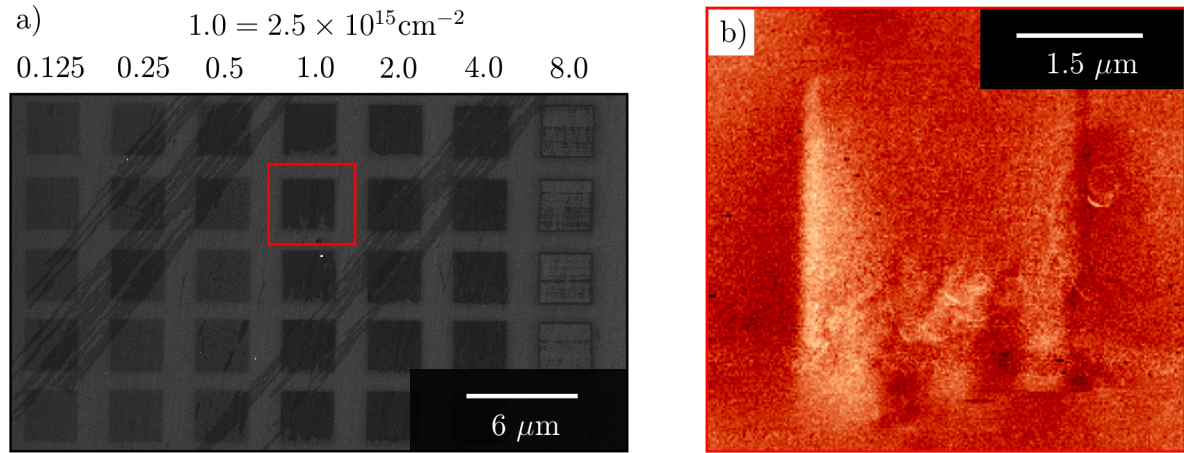


Figure 6.4: SEM and MFM analysis of an array of squares created by single scan of a 30 keV Ga beam with different doses.

Figure 6.5 shows a SEM/MFM analysis of FIB-treated surface of patterns which were created by scanning 100 times over the same area with 100 times lower dwell time. Because all of the parameters have been held similar to those in figure 6.4, we can see that the effect of multiple scans and a lower dwell time has an impact on the properties of the films. We can observe from the lowest dose that the irradiated areas have grain-like structures (a). A SEM-detail of one of the areas is portrayed in (b). The MFM analysis in (c) confirms that the square is transformed and contains magnetic dipoles [similar to those in figure 6.3(b)], which correspond very well to the SEM image of the same area (b).

6.2. MAGNETIC NANOSTRUCTURES CREATED BY 10 KEV GALLIUM IONS

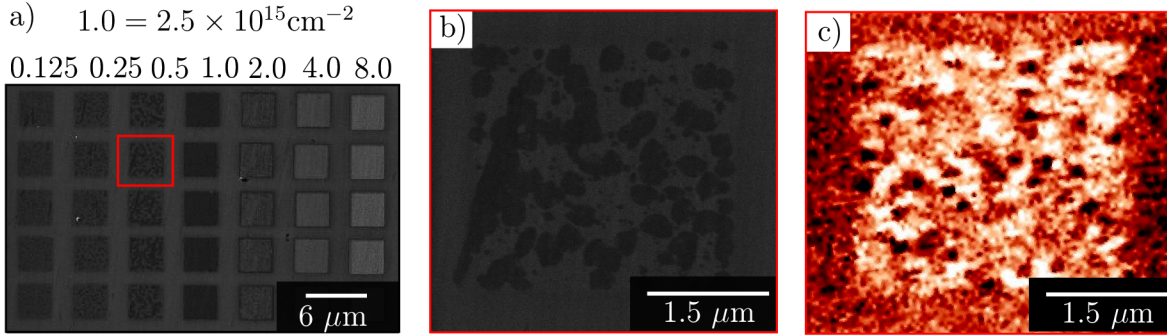


Figure 6.5: SEM/MFM analysis of FIB-treated surface of patterns, which were created by scanning 100 times over the same area with 100 times lower dwell time in comparison to 6.4.

6.2. Magnetic nanostructures created by 10 keV Gallium ions

From figure 6.1, it is clear that the ideal energy for ion-beam transformation of the Ga ions is 10 keV, because the ions have collision cascades confined to the 44 ML thick Fe₇₈Ni₂₂ and no FeNi-Cu intermixing takes place. The disadvantage of a beam with this energy is, however, that it loses its Gaussian shape and the irradiated nanostructures will therefore not have so well-defined spatial boundaries. We have investigated film irradiated with different ion doses, current and the number of scans. Results of these experiments are in figures 6.6, 6.7 and 6.8.

Let us first look at irradiation with a single scan with a high current (figure 6.6). The SEM analysis in (a) shows that all of the areas are transformed, even for lower ion doses. Their shape, however, is not as well-defined as in the event of 30 keV Ga ion irradiation. We can also see a “halo” around each square, which could be attributed to the typical pear-like interaction volume of incident ions 6.1. The MFM in (b) fully confirms the conclusions drawn from the SEM.

The effect of higher number of scans on the same area and a lower ion beam current is summarized in figure 6.7. The SEM and MFM again confirm that an increasing ion dose leads to an increased degree of film transformation. The irradiated squares however exhibit a different behaviour to the one described for single-scan, which was also observed for the films irradiated with 30 keV. The ion irradiation leads to a creation of bcc centres, which increase in size until the whole square is transformed.

An analysis of a square with bcc centres has been performed by AFM [figure 6.8(a)] and MFM (b). It can be argued, however, that the AFM signal does not come from the topography, but from the strong magnetic signal of the bcc domains, because if we compare the AFM profile to the MFM profile, they are extremely similar and the corrugation for the dose of $2.5 \times 10^{15} \text{cm}^{-2}$ is smaller. A decisive argumentation would, however, require a more thorough investigation, which was not a part of this thesis.

In conclusion to this chapter, we have shown we can fabricate magnetic nanostructures in the metastable films of Fe₇₈Ni₂₂/Cu(100). The data suggest that we dealt with a very interesting system, which offers a wide range of physics to explore.

6. MAGNETIC NANOSTRUCTURES IN 44 ML $Fe_{78}Ni_{22}$ FILMS

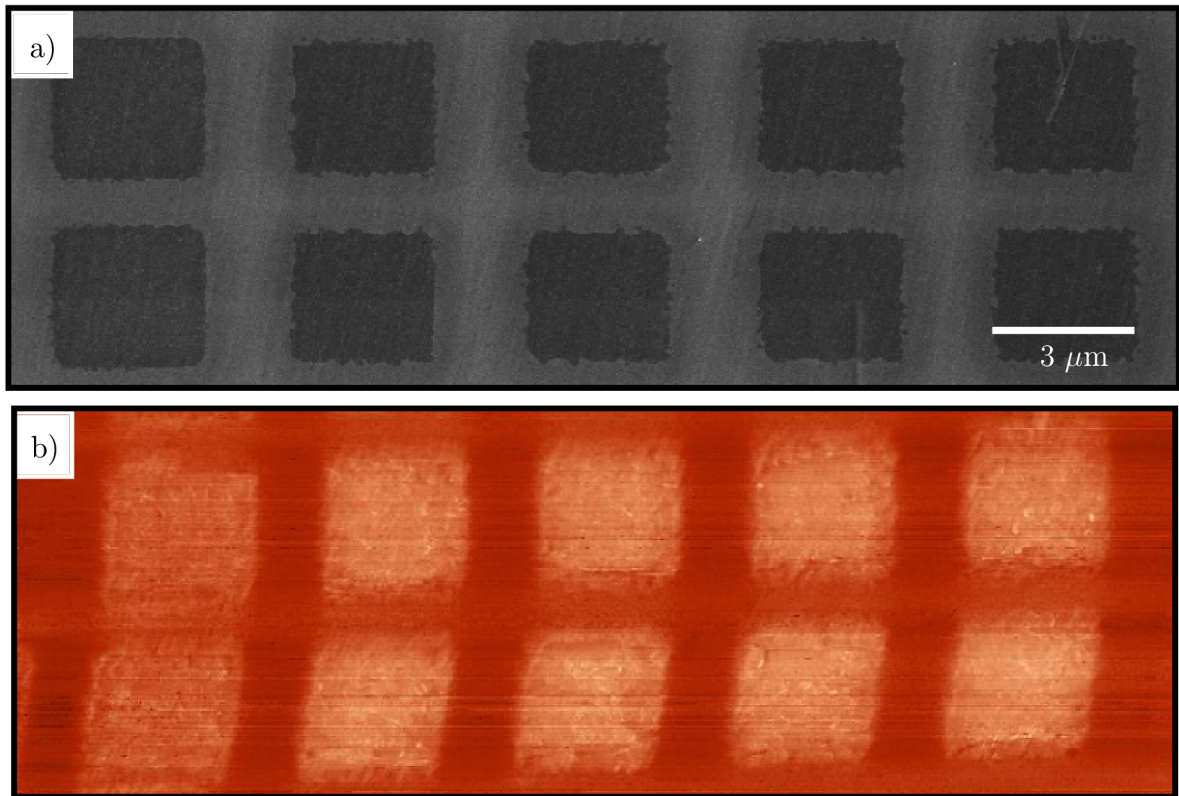


Figure 6.6: SEM and MFM analysis of areas irradiated by 10 keV Ga ions. The areas were transformed by single-scan beam with a current of 230 pA. Very similar properties can be observed for different doses. Doses were $(10, 5, 2.5, 1.25 \text{ and } 0.6) \times 10^{15} \text{ cm}^{-2}$ respectively.

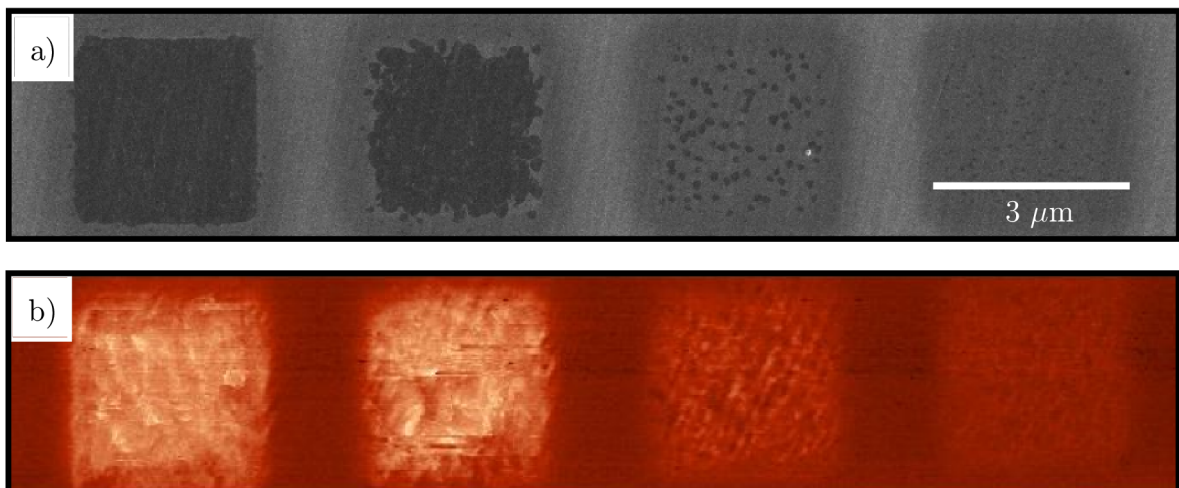


Figure 6.7: SEM and MFM analysis of areas irradiated by 10 keV Ga ions. The areas were transformed by 100 scans and the ion beam current was 32pA. Different magnetic properties can be observed for different doses. Doses were $(10, 5, 2.5 \text{ and } 1.25) \times 10^{15} \text{ cm}^{-2}$ respectively.

6.2. MAGNETIC NANOSTRUCTURES CREATED BY 10 KEV GALLIUM IONS

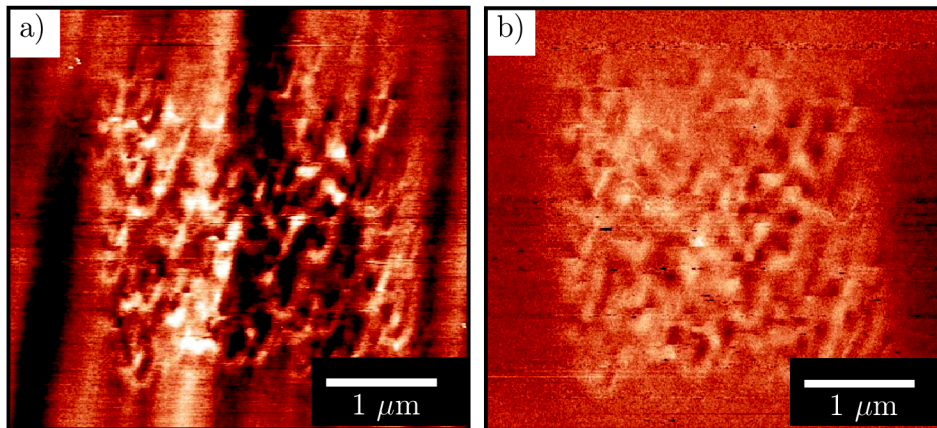


Figure 6.8: AFM and MFM analysis of a square with bcc centres. The irradiation was done by 100 scans with an ion beam current of 32 pA and the total ion dose of $2.5 \times 10^{15} \text{ cm}^{-2}$.

7. Conclusion

In this thesis we found the right ratio of a Fe-Ni alloy ($\text{Fe}_{78}\text{Ni}_{22}$), which allows the growth of metastable films without limitation in thickness on Cu(100) [6]. We have further demonstrated fabrication of magnetic nanostructures in these films. We have therefore confirmed and extended the results obtained by Shah Zaman [16] and proposed a novel system for nanoscale magnetic patterning of nano-magnetic devices and systems.

The review showed that our system is very interesting because it is one of few which gives the opportunity to create magnetic nanostructures embedded in non-magnetic matrix by means of ion-beam irradiation.

The outlook of this promising project is to further optimize the ion-beam irradiation parameters, because the LYRA microscope offers a tremendous space for variation with parameters which, as described in the last chapter, greatly affect the properties of the transformed film.

In order to obtain applications viable for the industry, the substrate used for the growth of our metastable films will have to be changed, because of its high price. The 8 nm thick films of $\text{Fe}_{78}\text{Ni}_{22}$ are very sensitive to oxidation and without a capping layer of, e.g. 2 nm Au can be used for experiments in ambient conditions (kept in low vacuum of a desiccator) only for a few days. Although the preliminary experiments at the TU Wien showed that we will be able to grow these metastable films at the BUT FME IPE, there is still rather a long way to go. We tried to conduct an experiment at the laboratories of our institute, but we stopped because of the problem with the sample orientation, which was not perpendicular to the incident electron beam from LEED in the Žeryk chamber. The Antonín UHV system can, however, serve as very good system for further investigation of the metastable Fe-Ni films.

We believe, that the system of $\text{Fe}_{78}\text{Ni}_{22}/\text{Cu}(100)$ is well described and understood and the fabrication of nanostructures in the films holds the potential worth future investigation.

Bibliography

- [1] A. Biedermann, M. Schmid, and P. Varga, “Nucleation of bcc iron in ultrathin fcc films,” *Phys. Rev. Lett.*, vol. 86, 2001.
- [2] W. Rupp, A. Biedermann, B. Kamenik, R. Ritter, C. Klein, E. Platzgummer, M. Schmid, and P. Varga, “Ion-beam induced fcc-bcc transition in ultrathin fe films for ferromagnetic patterning,” *Applied Physics Letters*, vol. 93, 2008.
- [3] S. S. Zaman, P. Dvořák, R. Ritter, A. Buchsbaum, D. Stickler, H. Oepen, M. Schmid, and P. Varga, “In-situ magnetic nano-patterning of Fe films grown on Cu(100),” *J. of Appl. Phys.*, vol. 110, p. 204309, 2011.
- [4] S. S. Zaman, H. Oßmer, J. Jonner, Z. Novotný, A. Buchsbaum, M. Schmid, and P. Varga, “Ion-beam-induced magnetic transformation of CO-stabilized fcc fe films on Cu(100),” *Phys. Rev. B*, vol. 82, 2010.
- [5] A. Biedermann, R. Tscheließnig, M. Schmid, and P. Varga, “Crystallographic structure of ultrathin fe films on cu(100),” *Phys. Rev. Lett.*, vol. 87, 2001.
- [6] J. Gloss, S. S. Zaman, J. Jonner, Z. Novotny, M. Schmid, P. Varga, and M. Urbanek, “Ion-beam-induced magnetic and structural phase transformation of Ni-stabilized face-centered- cubic Fe films on Cu(100),” *Appl. Phys. Lett.*, vol. 103, p. 262405, 2013.
- [7] M. Faraday, “The bakerian lecture: Experimental relations of gold (and other metals) to light,” *Phil. Trans. of the Royal Society of London*, vol. 147, p. 145, 1857.
- [8] M. Ohring, *The Materials Science of Thin Films*. Academic Press, 1991.
- [9] I. N. Stranski and L. Krastanov, “Abhandlungen der mathematisch - naturwissenschaftlichen klasse Iib.,” *Akad. Wiss. Wien*, vol. 146, p. 797, 1938.
- [10] J. C. Vickerman and I. S. Gilmore, *Surface Analysis - The Principal Techniques*. UK: John Wiley and Sons, second ed., 2009.
- [11] L. E. Davis, N. C. MacDonald, P. W. Palmberg, G. E. Riach, and R. E. Weber, *Handbook of Auger Electron Spectroscopy*. Physical Electronic Industries, Inc., second ed., 1976.
- [12] C. Davisson and L. Germer, “Diffraction of electrons by a crystal of Nickel,” *Phys. Rev. (2nd series)*, vol. 30, p. 705, 1927.
- [13] E. T. Whittaker, *A history of the theories of aether and electricity from the age of Descartes to the close of the 19th century*. Dublin University Press series. London: Longmans, Green and Co., 1910.
- [14] J. C. Maxwell, “Dynamical theory of the electromagnetic field.,” *Phil. Trans. of the Royal Society of London*, vol. 155, pp. 459–512, 1865.
- [15] E. F. Wassermann, *Ferromagnetic Materials*, vol. 5. North-Holland, Amsterdam, 2009.

- [16] S. S. Zaman, *Ion-beam induced magnetic nano-structures of Fe grown on Cu(100)*. PhD thesis, TU Wien, 2011.
- [17] S. Blomeier, P. Candeloro, B. Hillebrands, B. Reuscher, A. Brodyanski, and M. Kopnarski, “Ion-beam induced magnetic nanopatterning of interlayer exchange coupled Fe/Cr/Fe trilayers,” *J. Magn. Magn. Mat.*, vol. 310, 2007.
- [18] J. Kerr, “On reflection of polarized light from the equatorial surface of a magnet,” *Phil. Mag. Lett.*, vol. 5, pp. 161–171, 1878.
- [19] Z. Qiu and S. Bader, “SMOKE,” *J. Magn. Magn. Mat.*, vol. 100, pp. 440–454, 1991.
- [20] W. Rupp, *Ionenstrahl induzierter Ferromagnetismus von dünnen Fe-Schichten auf Cu(100)*. PhD thesis, TU Wien, 2009.
- [21] W. A. Jesser and J. W. Matthews, “Evidence for pseudomorphic growth of iron on copper,” *Philos. Mag.*, vol. 15, p. 1097, 1967.
- [22] P. B. K. Heinz, D. Mueller, “Iron multilayers on Cu(100) - a case of complex reconstruction investigated by quantitative LEED,” *Surf. Sci.*, vol. 352-354, pp. 942–950, 1996.
- [23] J. M. J. Fassbender, “Magnetic patterning by means of ion irradiation and implantation,” *J. Magn. Magn. Mat.*, vol. 320, p. 579–596, 2008.
- [24] P. Entel, E. Hoffmann, P. Mohn, K. Schwarz, and V. L. Moruzzi, “First-principles calculations of the instability leading to the Invar effect,” *Phys. Rev. B*, vol. 47, pp. 8706–8720, 1993.
- [25] W. Schilling and H. Ullmaier, “Physics of radiation damage in metals,” *Chemie, Weinheim*, vol. 10, p. 180, 1993.
- [26] A. Kirilyuk, J. Giergel, J. Shen, M. Straub, and J. Kirschner, “Growth of stabilized γ -Fe films and their magnetic properties,” *Phys. Rev. B*, vol. 54, pp. 1050–1062, 1996.
- [27] C. Chappert, “Planar patterned magnetic media obtained by ion irradiation,” *Science*, vol. 280, 1998.
- [28] G. Binnig and H. Rohrer, “Scanning tunneling microscopy,” *Helvetica Physica Acta*, vol. 55, pp. 726–435, 1982.
- [29] E. Meyer, H. Hug, and R. Bennewitz, *Scanning Probe Microscopy: The Lab on a Tip*. Advanced Texts in Physics, Springer, 2012.
- [30] J. Gierak, “Focused ion beam technology and ultimate applications,” *Semiconductor Science and Technology*, vol. 24, 2009.
- [31] M. Urbánek, V. Uhlír, P. Bátor, E. Kolíbalová, T. Hrnčíř, J. Spousta, and T. Sikola, “Focused ion beam fabrication of spintronic nanostructures: an optimization of the milling process.,” *Nanotechnology*, vol. 21, no. 14, 2010.

BIBLIOGRAPHY

- [32] I. N., *Interactions of ions with matter*. Cambridge: Cambridge University Press, focused ion beam systems: basics and applications ed., 2007.
- [33] J. Fassbender, J. von Borany, A. Mücklich, K. Potzger, W. Möller, J. McCord, L. Schultz, and R. Mattheis, “Structural and magnetic modifications of Cr-implanted permalloy,” *Phys. Rev. B*, vol. 73, p. 184410, May 2006.
- [34] J. Fassbender, A. Mücklich, K. Potzger, and W. Möller, “Mixing and subsequent amorphization of ultrathin Ni₈₁Fe₁₉/Ta bilayers by 30keV ni implantation,” *Nuclear Instruments and Methods in Physics Research Section B: Beam Interactions with Materials and Atoms*, vol. 248, 2006.
- [35] M. Martín-González, F. Briones, J. García-Martín, J. Montserrat, L. Vila, G. Faini, A. Testa, D. Fiorani, and H. Rohrmann, “Nano-patterning of perpendicular magnetic recording media by low-energy implantation of chemically reactive ions,” *J. Magn. Magn. Mat.*, vol. 322, 2010.
- [36] D. Ravelosona, J. Menendez, J. Attane, H. Bernas, D. Halley, K.-H. Heinig, A. Marty, P. Auric, C. Chappert, and Y. Samson, “Ordering intermetallic alloys by ion irradiation: a new way to tailor magnetic media,” *Magnetics Conference INTERMAG 2003.*, pp. DE-08, 2003.
- [37] A. F. C. Chappert and F. N. Dau, “The emergence of spin electronics in data storage,” *Nature Materials*, vol. 6, pp. 813–822, 2007.
- [38] E. Menéndez, M. O. Liedke, J. Fassbender, T. Gemming, A. Weber, L. J. Heyderman, K. V. Rao, S. C. Deevi, S. S. ach, M. D. Baró, J. Sort, and J. Nogués, “Direct magnetic patterning due to the generation of ferromagnetism by selective ion irradiation of paramagnetic FeAl alloys,” *small*, vol. 5, pp. 229–234, 2009.
- [39] H. Bernas, J.-P. Attané, K.-H. Heinig, D. Halley, D. Ravelosona, A. Marty, P. Auric, C. Chappert, and Y. Samson, “Ordering intermetallic alloys by ion irradiation: A way to tailor magnetic media,” *Phys. Rev. Lett.*, vol. 91, 2003.
- [40] T. Devolder, “Light ion irradiation of co/pt systems: Structural origin of the decrease in magnetic anisotropy,” *Phys. Rev. B*, vol. 62, pp. 5794–5802, 2000.
- [41] S. Maat, A. Kellock, D. Weller, J. Baglin, and E. Fullerton, “Ferromagnetism of FePt₃ films induced by ion-beam irradiation,” *J. Magn. Magn. Mat.*, vol. 265, pp. 1–6, 2003.